論文 / 著書情報
Article / Book Information

Title	Electrical image of subduction zone beneath northeastern Japan
Authors	Masahiro Ichiki, Yasuo Ogawa, Toshiki Kaida, Takao Koyama, Makoto Uyeshima, Tomotsugu Demachi, Satoshi Hirahara, Yoshimori Honkura, Wataru Kanda, Toshio Kono, Masaki Matsushima, Takashi Nakayama, Syuichi Suzuki, Hiroaki Toh
Citation	Journal of Geophysical Research, , ,
Pub. date	2015, 12
Copyright	Copyright (c) 2015 American Geophysical Union (AGU)
Creative Commons	See next page.

License

AGU PUBLICATIONS

JGR

Journal of Geophysical Research: Solid Earth

RESEARCH ARTICLE
10.1002/2015JB012028

Key Points:
- Flow overturn toward the back arc in the mantle wedge is imaged by resistivity
- Fluid pathways from the slab top to lower crust are revealed beneath NE Japan
- The lower crust conductor requires at least 0.7 vol. % of fluid fraction

Supporting Information:
- Texts S2, S3, and S5, and Figures S1 and S3–S5

Correspondence to:
M. Ichiki,
ichiki@m.tohoku.ac.jp

Citation:
Ichiki, M., et al. (2015), Electrical image of subduction zone beneath northeastern Japan, *J. Geophys. Res. Solid Earth*, *120*, doi:10.1002/2015JB012028.

Received 11 MAR 2015
Accepted 1 OCT 2015
Accepted article online 8 OCT 2015

Electrical image of subduction zone beneath northeastern Japan

Masahiro Ichiki[1], Yasuo Ogawa[2], Toshiki Kaida[1], Takao Koyama[3], Makoto Uyeshima[3], Tomotsugu Demachi[1], Satoshi Hirahara[1], Yoshimori Honkura[2,4], Wataru Kanda[2], Toshio Kono[1], Masaki Matsushima[4], Takashi Nakayama[1], Syuichi Suzuki[1], and Hiroaki Toh[5]

[1]Graduate School of Science, Tohoku University, Sendai, Japan, [2]Volcanic Fluid Research Center, Tokyo Institute of Technology, Tokyo, Japan, [3]Earthquake Research Institute, University of Tokyo, Tokyo, Japan, [4]Graduate School of Science and Engineering, Tokyo Institute of Technology, Tokyo, Japan, [5]Graduate School of Science, Kyoto University, Kyoto, Japan

Abstract We conducted long-period magnetotelluric observations in northeastern Japan from 2010 to 2013 to investigate the three-dimensional electrical resistivity distribution of the subduction zone. Incorporating prior information of the subducting slab into the inversion scheme, we obtained a three-dimensional resistivity model in which a vertically continuous conductive zone is imaged from the subducting slab surface to the lower crust beneath the Ou Backbone Range. The conductive body indicates a saline fluid and/or melt pathway from the subducting slab surface to the lower crust. The lower crust conductor is less than 10 Ω m, and we estimate a saline fluid and/or melt fraction of at least 0.7 vol. %. Other resistivity profiles in the across-arc direction reveal that the conductive body segregates from the subducting slab surface at 80–100 km depth and takes an overturned form toward the back arc. The head of the conducting body reaches the lower crust just beneath Mt. Gassan, one of the prominent back-arc volcanoes in the system.

1. Introduction

Water in the deep earth accelerates the strain rate of mantle silicates and diminishes the solidus temperature [e.g., *Mei and Kohlstedt*, 2000a, 2000b; *Green*, 1973]. In this sense, water plays a key role in mantle dynamics and magma generation. Presumably, water inside the earth is supplied mostly from subduction zones, which is estimated to be 870–1000 Tg/yr of water [*Peacock*, 1990; *van Keken et al*., 2011]. Many earthquakes and volcanic eruptions develop around subduction zones, which are affected by fluids released from the slabs. Investigations to determine the distribution of fluids in the mantle wedge are pertinent for revealing fluid transport after dehydration of the subducting slab and for accounting for earthquakes and volcanic activity.

Northeastern Japan (NEJ) contains a well-studied subduction system and is an ideal place to use magnetotelluric (MT) methods to delineate melt and fluid transport. To delineate the fluid distribution in the mantle wedge beneath NEJ, we performed a three-dimensional (3-D) electrical resistivity (or conductivity) study. Long-period (longer than 10^3 s) geomagnetic transfer functions and magnetotellurics (MT) in NEJ have been widely observed during the 1970s and 1980s [see *Kanda and Ogawa*, 2014, and references therein]. Incorporating the ocean bathymetry and sea water into the models, *Ogawa et al*. [1986] and *Utada* [1987] proposed two-dimensional (2-D) resistivity models in the crust and upper mantle beneath NEJ for the first time. Since the 1990s, Network-MT observation targeting the upper mantle has been expanded to NEJ [*Uyeshima et al*., 2002]. However, these previous studies analyzed the data over a limited number of periods and could only identify uniform resistivity in the mantle wedge beneath NEJ. This study collected MT data in the wide period range (20–61,440 s) and provides a more detailed view of the resistivity distribution in the mantle wedge beneath NEJ.

It is well known that fluids in the upper mantle have various types of configurations, such as supercritical fluid at grain boundaries, hydrogen in nominally anhydrous minerals, and fluid inclusions. Electrical conductivity measurements of mantle silicates under wet and dry conditions in laboratory experiments have revealed that electrical conductivity is consistently sensitive to the presence of water irrespective of configuration [e.g., *Karato*, 1990; *Jödicke*, 1992; *Yoshino et al*., 2006]. Recent 3-D MT, particularly of the USArray project, have revealed rippled conductors around the Moho depth in map view [e.g., *Patro and Egbert*, 2008; *Kelbert et al*., 2012; *Meqbel et al*., 2014]. The conductors are interpreted as saline fluids and/or melt (hereafter denoted as fluid/melt) associated with underplating [e.g., *Wannamaker et al*., 2008]. In this paper, we show some

conductive plumes in the crust and upper mantle below NEJ, which correspond well with active volcanoes at the surface. The conductive plumes indicate fluid/melt pathways from the surface of the subducting slab to lower crust conductors. One of the pathways appears very specific and seems to be associated with the back-arc volcanism. We discuss this result and the implications of this specific pathway later in the paper.

In the following section, we first give an overview of the tectonic settings of NEJ and summarize the long-period MT experiments, data processing, and distortion analysis of the MT. Section 3 describes how we adapted the 3-D inversion framework to the subduction zone. Section 4 describes the obtained resistivity structure and its key features. Section 5 describes the sensitivity tests for the key features using the Fréchet derivative and boxcar test, and then we discuss all the results and conclude this paper in sections 6 and 7.

2. Experiment

2.1. Outline of Tectonic Settings

NEJ is located on the Okhotsuk plate in the MOVEL model [*DeMets et al*., 2010]. Beneath the Okhotsuk plate, the Pacific plate subducts at a dip angle of about 30° and at a rate of 8–9 cm/yr [e.g., *Cruciani et al*., 2005]. Below NEJ, the Pacific plate is very cold and old (~130 Ma), and its thickness has been estimated to be about 90 km by seismic receiver function [*Kawakatsu et al*., 2009]. A prominent orogenic belt called the Ou Backbone Range (OBR) runs through central NEJ in the along-arc direction (Figure 1). The OBR likely developed by crustal softening owing to fluids squeezed from the magma chamber in the lower crust and by upthrust caused by the principal regional stress axis that is parallel to the across-arc direction [e.g., *Hasegawa et al*., 2005]. In this paper, the back arc and fore arc are defined as the Japan Sea side and Pacific Ocean side of the OBR. Active Quaternary volcanoes in NEJ are concentrated along OBR. However, there exists some enigmatic Quaternary volcanism in the back-arc region [e.g., *Tatsumi*, 1989]. *Tamura et al*. [2002] pointed out that the back-arc volcanism is located on some zonal clusters of volcanoes in the across-arc direction (Figure 1). They called the zonal clusters hot fingers. Volcanism on each hot finger track likely developed with a 70–80 km eastward migration in the last 5 Ma [*Kondo et al*., 2004; *Honda and Yoshida*, 2005].

2.2. Observation and MT Response

Long-period MT data were acquired at 59 land sites in NEJ (Figure 1) by the GEOFLUID project in Japan (http://www.geofluids.titech.ac.jp/eng/index_e.html). The dimensions of the survey area are 150 × 200 km in the north-south (N-S) and east-west (E-W) directions, respectively, and the typical spacing between sites is 20 km. Either a LEMI-417M or NIMS system, using a fluxgate magnetometer, was installed at each land site during a 2-to-4 month time period. The sampling rate was 1 Hz. Telluric field variation was recorded with a dipole length of 40 m using Pb-$PbCl_2$ electrodes. The installation of the electrodes was performed by using a magnetic compass, and so the obtained electric field data are assumed to have been oriented to local geomagnetic coordinates. We carefully maintained the level of the fluxgate magnetometers and kept the magnetic *y* component within plus or minus a few hundred nanoteslas when installing the sites. The magnetic field data at eight sites were acquired using LEMI-417M gimballed fluxgate magnetometers, but the fluxgate magnetometers at 51 sites were not gimballed.

To remove tilt changes, baseline steps, and drifts of the fluxgate magnetometers, we first subtracted magnetic field variations to which a median filter was applied from raw data (Figure S1 of the supporting information). The time-window width of the median filter was 1 day. To delineate the response of the median filter, we calculated the power spectrum density (PSD) of magnetic field variation before and after the demedian operation. The test magnetic field variation was acquired using a gimballed fluxgate magnetometer. The PSD revealed that the demedian operation eliminated natural magnetic field variations at periods longer than 1 day as well as tilt changes, baseline steps, and drifts, whereas it did not modify the nature of the magnetic field variation in periods shorter than 1 day (Figure S1). Henceforth, period ranges longer than 1 day are not dealt with in this paper. The horizontal coordinate of the fluxgate magnetometer at each site should be somewhat rotated from the local geomagnetic coordinate depending on the local time of installation and on the installation itself. We rotated the horizontal coordinate so that the declination of the observation coordinate coincided with that of the reference local geomagnetic coordinate. The declination of the observation coordinate at each site was calculated from the median filtered data at the beginning of

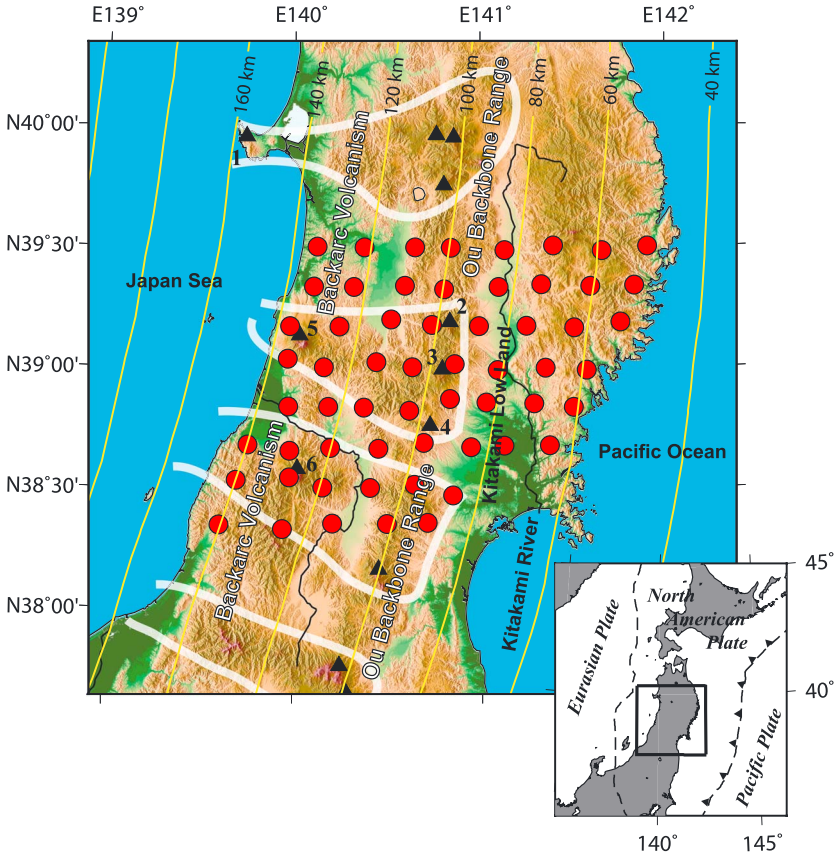

Figure 1. Observation site superimposed on morphological and geophysical background of NEJ. Circle shows the MT observation sites. The triangle shows volcanoes and the numbering volcanoes are mentioned in the text: 1. Ichinomegata Maar, 2. Mt. Yakeishi, 3. Mt. Kurikoma, 4. Mt. Naruko, 5. Mt. Chokai, and 6. Mt. Gassan. Most arc volcanoes are aligned north to south at the center of the northeastern Japan arc, which is called the Ou Backbone Range. Mts. Chokai and Gassan are located in the back-arc side from the Ou Backbone Range. These are defined as back-arc volcanism in this paper. Back-arc volcanism is located along some zonal volcano clusters delineated by white line. The zonal volcano distribution is called hot fingers [*Tamura et al.*, 2002]. Yellow lines show isodepths of subducting Pacific plate surface [*Kita et al.*, 2010; *Nakajima and Hasegawa*, 2006]. Solid lines are permanent major rivers. *Child map*: Plate boundaries around study area. Dashed line shows the plate boundary. Rectangle surrounded by thick solid line represents the region of the main figure. Pacific plate subducts beneath North American plate.

observation because the beginning of each observation was expected to have been performed on leveled coordinates. The reference local geomagnetic declination at each site was obtained from interpolation of grid data of Geomagnetic Chart 2010 observed by the Geospatial Information Authority of Japan (http://vldb.gsi.go.jp/sokuchi/geomag/menu_04/index-e.html). The grid width is 3 min.

The obtained electromagnetic field variation data were processed into MT responses with the bounded influence robust remote reference processing code (BIRRP) [*Chave and Thomson*, 2004]. We calculated the MT responses for all sites at 20 and 30 s and their overtone periods up to 40,960 and 61,440 s (24 periods in total). Each site had three to seven adjacent sites that simultaneously observed the electromagnetic field. We selected the site that had the best quality data among those sites as a remote reference. A 20 km separation between target and remote reference site is sufficient to obtain good quality MT responses in the period range of 30 to 20,000 s because of the high fidelity electromagnetic signals measured in NEJ. Figure 2 shows the spatial distribution of the MT nondiagonal phase response at periods of 320, 1920, 5120, and 15,360 s. The P_{yx} represents the characteristics of the E-W telluric current that is nearly perpendicular to the Japan Trench. The P_{yx} distribution at a period of 320 s shows several isolated patches corresponding to local crustal heterogeneity. At periods of 1920 and 5120 s, a low-P_{yx} domain of less than −135° occurs to the east and a high-P_{yx} domain of more than −135° occurs to the west of OBR. A few patches that correspond to complex heterogeneity around Mts. Yakeishi, Kurikoma, Naruko, and Gassan are superimposed on the background.

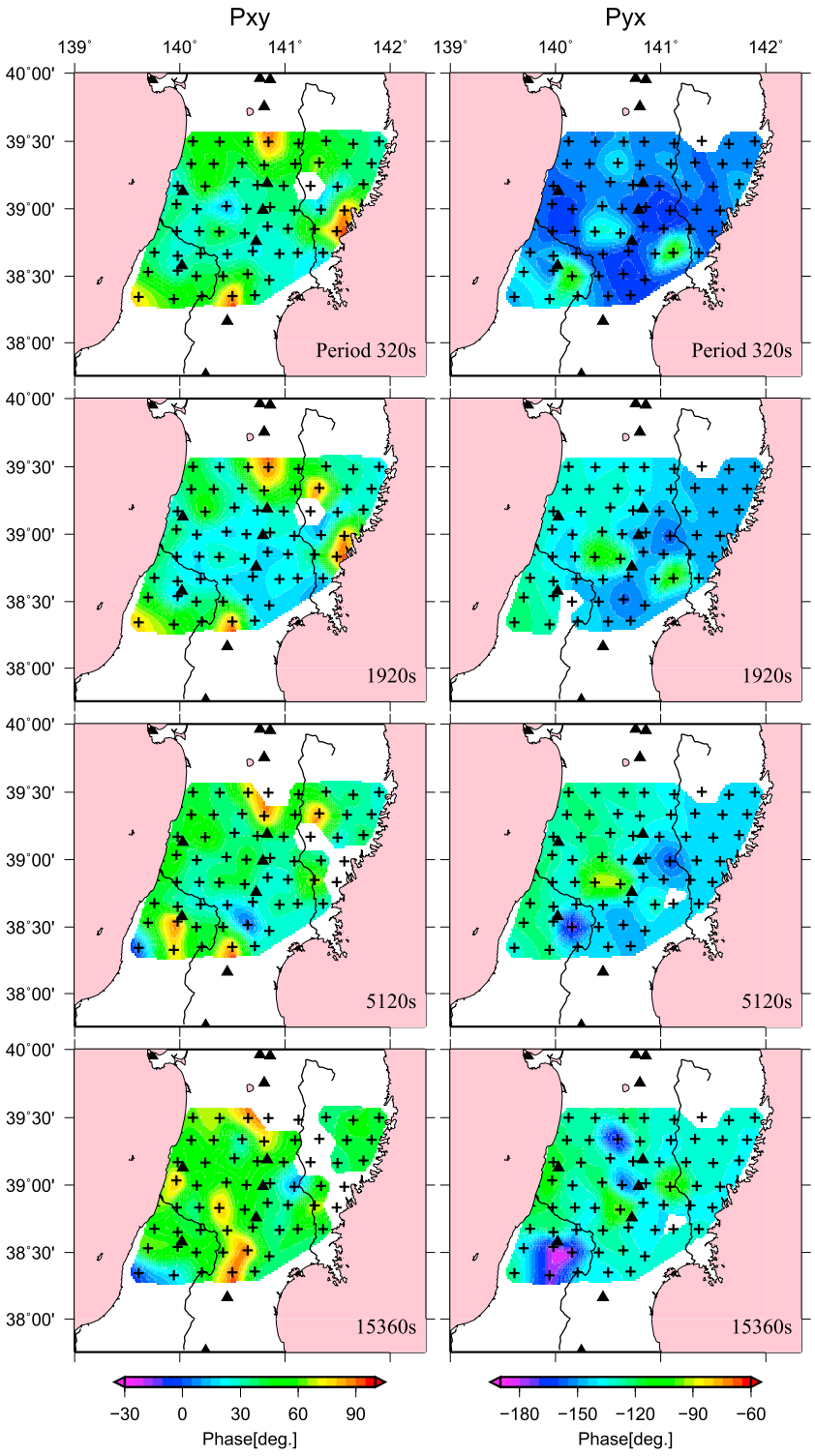

Figure 2. Spatial distribution of MT nondiagonal phase response at the periods of 320, 1920, 5120, and 15,360 s. Left and right columns show P_{xy} and P_{yx} distribution, respectively. The P_{xy} is MT phase response between electric field in the north-south component and magnetic field in the east-west component, and P_{yx} is that between electric field in the east-west component and magnetic field in the north-south component. Cross represents observation site. The spatial distribution is drawn using cosine arch filtering with 20 km width (use of "grdfilter" in GMT) [*Wessel and Smith*, 1998].

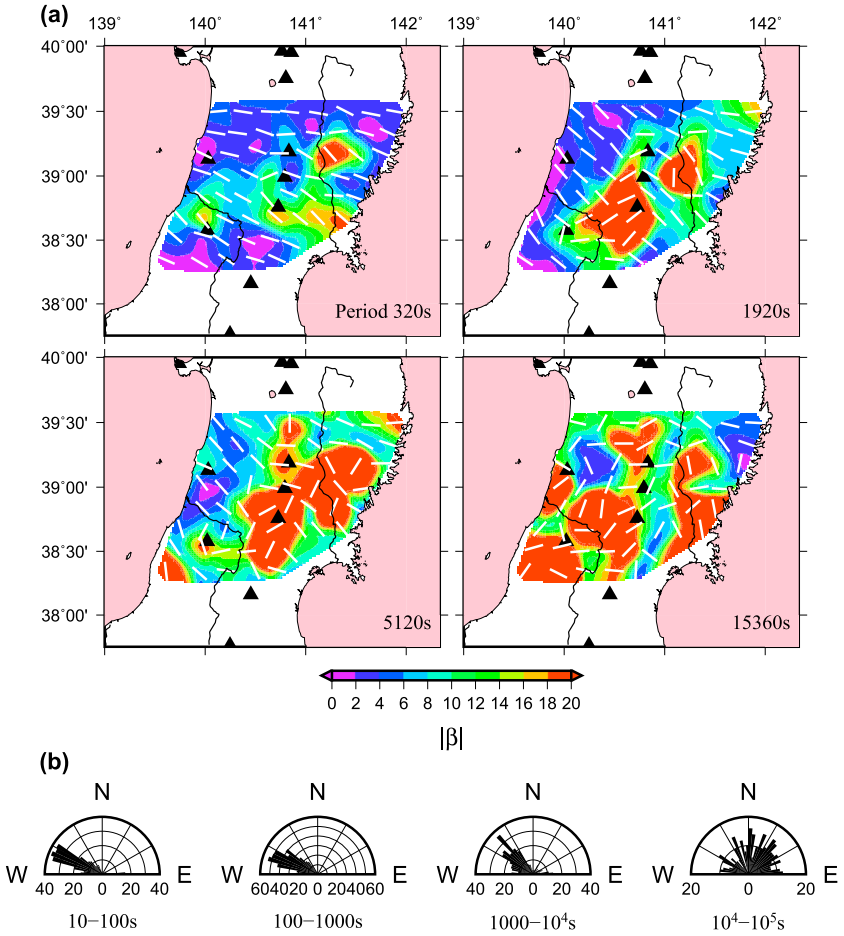

Figure 3. (a) Spatial distribution of the skew angle (β angle) and reference axis direction of the phase tensor at the periods of 320, 1920, 5120, and 15,360 s. The background color shows the β angle distribution drawn by the same means of Figure 2. White bar direction shows the reference axis direction at each site and period. The length is arbitral. (b) Rose diagram of the reference axis direction in each period range.

Although the phase tensor analysis revealed that the conductivity distribution is entirely 3-D in this study region (described later), this spatial background distribution of P_{yx} indicates a regional two-dimensional image in which a cold and electrically resistive subducting slab lies to the east and a warm and conductive mantle wedge is located in the west. At 15,360 s, the P_{yx} distribution no longer assumes a two-dimensional pattern. In contrast to the P_{yx} distribution, the P_{xy} spatial distribution is dominantly affected by the 3-D character inherent in the study region.

2.3. Dimensionality Analysis

The MT response is distorted by the static electric field caused by charge buildup at boundaries of local surficial conductivity heterogeneity around the observation site, which are smaller than the shortest skin depth [e.g., *Jiracek*, 1990]. Hence, the phase tensor, which is calculated from the MT response but which is not influenced by galvanic effect, is often used to highlight details of the conductivity distribution as a function of period (or depth) [*Caldwell et al.*, 2004; *Bibby et al.*, 2005]. The skew angle β and reference axis α of the phase tensor allow us to probe the dimensionality of the conductivity distribution [*Bibby et al.*, 2005]. Figure 3a shows the phase tensor reference axis of each site superimposed on the spatial distribution of skew angle magnitude at the same periods used in Figure 2. The regions around Mts. Yakeishi, Kurikoma, Naruko, and Gassan and Kitakami Low Land show larger skew angle magnitudes of more than 10° throughout the period range of 10 to 10^5 s. This suggests a 3-D resistivity distribution in the crust and upper mantle around these active volcanoes and the Kitakami River. In other areas, small skew angle magnitudes of less

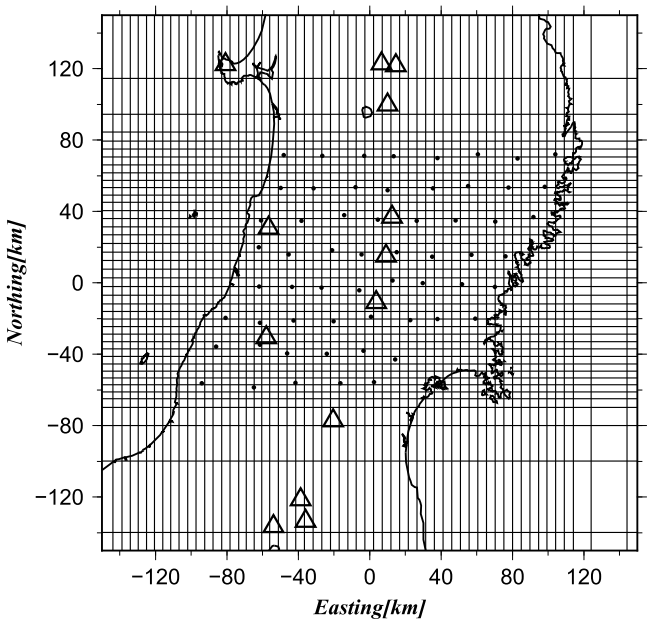

Figure 4. Horizontal mesh in the central region of model space. Black dot and open triangle represent observation site and volcano, respectively.

than 5° are dominant in the period range of 10 to 1000 s. Hence, the crusts outside of the volcanic regions and the Kitakami River are consistent with a two-dimensional resistivity distribution. The skew angle magnitude increases over the entire region at periods over 1000 s. The rose diagram of reference axis direction (Figure 3b) provides a clearer image of these trends. Note that there is a 90° ambiguity in strike direction to the reference axis. In the period range of 10 to 1000 s, the statistics of the reference axes have a distinctive modal direction of west-northwest. This indicates a two-dimensional resistivity distribution in correspondence with the skew angle result. A small amount of scattering of the reference axis direction is seen in the period range of 10 to 1000 s. This scattering stems mainly from the data in the 3-D conductivity region of the active volcanoes and Kitakami River area, as described above. An obvious modal direction is observed in the period range of 1000 to 10^4 s. However, it is rotated about 30° clockwise from the modal direction in the period range of 10 to 1000 s. Furthermore, a large skew angle magnitude region covers the area in the period range of 1000 to 10^4 s (see the 5120 s period illustration in Figure 3a). At periods of more than 10^4 s, the reference axis directions are completely random statistics. Consequently, no consistent reference axis direction exists throughout the period range of 10 to 10^5 s. Moreover, the spatially wide and periodic distribution of large skew angle magnitude reveals the 3-D feature of the study area. Hence, 3-D analysis and interpretation are appropriate for this data set.

3. Inversion

3.1. Outline of the Inversion

The input data set for the subsequent 3-D inversion was arranged depending on the data quality. We excluded the MT impedance data for which the standard error (SE) was infinity or was "not a number" in the output of BIRRP processing from the input data set. We also eliminated extreme outlier MT impedances. Here extreme outlier means that the two-sided twice SE ranges lie away from the main trend of the MT impedance response curve as a function of period. The error floors were all assigned as 10% of each individual impedance component throughout the inversion process. Because of the limitation of our computer resources, we used the MT impedances at 30 s and its harmonics up to 61,440 s (12 periods). Note that we confirmed that the use of the MT impedances at the alternative 12 periods (20 s and its harmonics) gave the same conductivity models and the root-mean-squared misfits normalized by the standard errors (hereafter denoted as RMS misfits).

The 3-D inversion was carried out by using WSINV3D-MPI-1.2 [*Siripunvaraporn et al.*, 2005; *Siripunvaraporn and Egbert*, 2009]. The WSINV3D seeks a likelihood model giving a stationary point of the following functional U:

$$U(\mathbf{m},\lambda) = (\mathbf{m}-\mathbf{m}_0)^{\mathrm{T}}\mathbf{C_m}^{-1}(\mathbf{m}-\mathbf{m}_0) + \lambda^{-1}\left[(\mathbf{d}-F[\mathbf{m}])^{\mathrm{T}}\mathbf{C_d}^{-1}(\mathbf{d}-F[\mathbf{m}])\right], \quad (1)$$

where $\mathbf{m}$ is the conductivity model, $\mathbf{m}_0$ is the reference or prior model, $\mathbf{C_m}$ is the model covariance matrix [*Siripunvaraporn and Egbert*, 2000], $\mathbf{d}$ is the observed data, $F[\ ]$ is the forward operator, $\mathbf{C_d}$ is the data covariance matrix, and λ^{-1} is the Lagrange multiplier. The first term is called the regularization or penalty term. We describe more details of WSINV3D and its algorithms in the supporting information.

Figure 4 shows the mesh distribution in the central model space. The total model space domain is ±700 km in the N-S direction, ±744 km in the E-W direction, and 1200 km in depth. The finest width of the lateral mesh is 3.8 km.

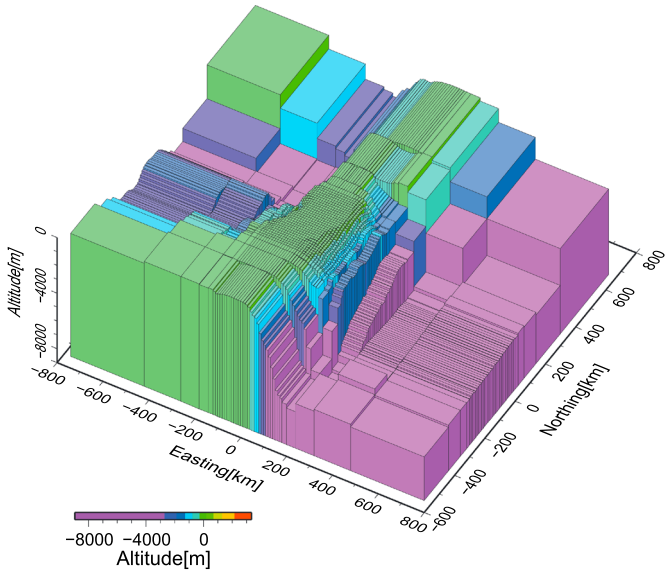

Figure 5. Bird's eye view of ocean bathymetry employed in the inversion.

The surface vertical grids down to 1 km are 100, 200, 400, and 600 m. The total number of meshes is $47 \times 66 \times 57$ (with seven air layers) = 176,814. Ocean bathymetry (ETOPO1) and seawater resistivity (0.33 Ω m) were fixed and incorporated beforehand into all models (Figure 5). The total number of unknown model parameters was 148,938.

3.2. Search for Reference Model and Model Covariance Parameters

We took the following three steps in the inversion to obtain the highest likelihood conductivity model: (a) search for the best reference model by trial and error using the default model covariance parameters, (b) search for the optimal model covariance parameters using the best reference model obtained in (a), and (c) complement the search for the reference model by using model covariance parameters other than the default ones in (a).

In the first step, we gave $\tau = 1$, $\delta i = 0.5$ ($i = x, y, z$) to the default model covariance parameters. Here $4\tau\delta_i$ ($i = x, y, z$) gives a model covariance width or model smoothness in x, y, and z directions (see supporting information). The reference model, $\mathbf{m}_0$, in the regularization term of equation (1) is requisite in the MT inversion targeting the subduction zone. The regularization term in the form of λ^{-1} **Lm** without the reference model is the most popular [e.g., *Constable et al*., 1987; *Uchida*, 1993]. Here **L** is a finite difference matrix of the model parameters between laterally and vertically adjacent blocks (smoothness constraint). This regularization form without the reference model has successfully overcome unstable and/or unrealistic solutions in many cases; however, when we use the regularization term without the reference model for a subducting slab and mantle wedge, the inversion usually provides only a less-informative model in which the electrically resistive region corresponding to the subducting slab is widely blurred [e.g., *Toh et al*., 2006; *Matsuno et al*., 2010]. This is ascribed to an MT response insensitive to the surface boundary of the resistive block [e.g., *Torres-Verdin and Bostick*, 1992]. To avoid recovering such models, we experimented with assigning the surface boundary and thickness of the subducting slab to the reference model. Accordingly, we attempted three types of reference models in operating the 3-D inversion. The model types were uniform models (five models), layered models (five models), and models incorporating the subducting slab into the layered model (hereafter denoted as slab models; four models). The reference models attempted are shown in Figure 6 and Table 1. The resistivities of the attempted uniform reference models were 5000, 1000, 500, 100, and 10 Ω m. The boundaries of the layered models were fixed at depths of 40 (crust), 200 (shallow upper mantle), and 400 (deep upper mantle) km. The resistivities of the deep upper mantle and mantle deeper than 400 km were fixed at 10 and 1 Ω m, respectively. The slab models were composed of the best layered model and the subducting slab. The slab geometry was assigned by referring to the upper boundary of the subducting Pacific plate below NEJ defined by the seismicity [*Kita et al*., 2010; *Nakajima and Hasegawa*, 2006] and to the Pacific plate thickness of 90 km [*Kawakatsu et al*., 2009]. We experimented with 1000, 5000, 10 k, and 20 k Ω m of slab resistivity. The best reference model was selected using the following rules. (1) The reference model giving a minimum RMS misfit was selected as optimal when no inversion attained stage II of the Occam process. (2) When there were multiple types of reference models that progressed inversion to stage II, we adopted the model in which more prior information was incorporated as the best reference model.

The next step was to determine the optimal model covariance parameters using the best reference model obtained in the first step. We adopted the model covariance parameters that gave the minimal RMS misfit. Here the attempted values of $4\tau\delta_i$ were 0.5, 1.0, 2.0 (default), 4.0, and 8.0. In this step, we removed the scheme of stage II of the Occam process. Generally, there likely exists a minimal RMS misfit as a function of model

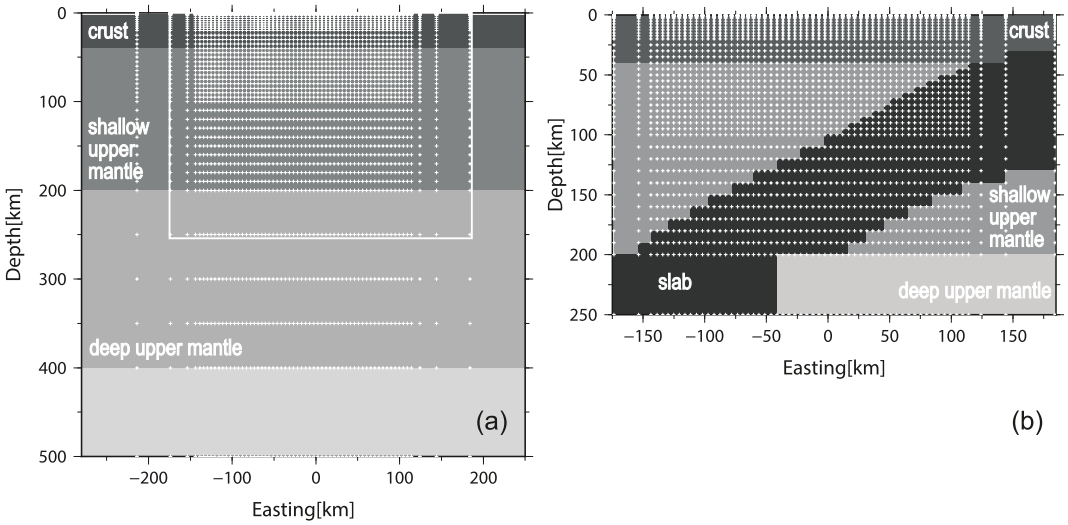

Figure 6. Schematic view of vertical profile of (a) layered and (b) slab reference model in east-west direction. White cross indicates grid point. White line box in Figure 6a corresponds to the domain of Figure 6b.

covariance parameters in the WSINV3D inversion. We confirmed this fact by using two synthetic data sets; the example data given by *Siripunvaraporn et al*. [2005] and the other were calculated from a model in which a single conductive cube was embedded in the best reference model (see supporting information). *Aizawa et al*. [2014] also indicated that there was a minimal RMS misfit as a function of model covariance parameters in their data set.

In the third step, we considered the dependence of the best reference model on the model covariance parameters. In the first step, the best reference model was evaluated by using $4\tau\delta_i = 2.0$. If we started the three steps using different model covariance parameters, another reference model might be adopted, and it might possibly give a smaller RMS misfit. Hence, we looked for a likelihood model in the model domain that was far from the search range in steps 1 and 2. Specifically, we repeated step 1 using $4\tau\delta_i = 0.5$ and 8.0, the two cases of extreme model covariance parameter, respectively. Then we confirmed whether the best reference model was changed and whether the RMS misfit fell below the smallest RMS misfit obtained in the second step.

Table 1. Attempted Reference Resistivity Models[a]

Model Type	Model ID	Crust (0–40 km Depth)	Shallow Upper Mantle (40–200 km Depth)	Deep Upper Mantle (200–400 km Depth)	400–1200 km Depth	Slab
Uniform	1	5000	5000	5000	5000	–
	2	1000	1000	1000	1000	–
	3	500	500	500	500	–
	4	100	100	100	100	–
	5	10	10	10	10	–
Layered	6	1000	100	10	1	–
	7	500	100	10	1	–
	8	1000	10	10	1	–
	9	500	10	10	1	–
	10	100	10	10	1	–
Slab	11	1000	100	10	1	1000
	12	1000	100	10	1	5000
	13	1000	100	10	1	10 k
	14	1000	100	10	1	20 k

[a]Unit in Ωm. See text and Figure 6 for detail.

Table 2. The Best RMS Misfit of the Inversion Using Various Kinds of Reference Models[a]

		$4\tau\delta i = 2.0$			$4\tau\delta i = 0.5$			$4\tau\delta i = 8.0$		
Model Type	Model ID	Iteration	λ	RMS Misfit	Iteration	λ	RMS Misfit	Iteration	λ	RMS Misfit
Uniform	1	5	−1.0	3.75	4	−0.5	6.05	7	−1.5	4.17
	2	7	−0.5	2.81	3	0.0	3.32	2	−3.0	4.77
	3	4*	−0.5*	3.01*	3*	0.0*	3.28*	5	−1.0	3.66
	4	3	−0.5	3.18	8	0.0	3.08	4	−1.5	3.49
	5	1	−1.0	3.75	1	−0.5	3.65	3	−1.5	3.74
Layered	6	8	−0.5	2.72	7*	0.0*	3.41*	7	−1.5	3.26
	7	9	−0.5	2.85	3	0.0	3.33	6	−1.5	3.35
	8	9*	0.0*	2.95*	3*	0.5*	3.61*	6	−1.5	3.34
	9	7	−0.5	3.11	3	−0.5	3.89	6	−1.5	3.32
	10	6	−0.5	3.48	2	0.0	3.47	3	−1.5	3.53
Slab	11	7	−0.5	2.66	3	0.0	3.26	4*	−1.0*	3.27*
	12	5	−0.5	2.48	3	0.5	2.88	4	−1.0	3.34
	13	5	−0.5	2.47	3	0.0	3.08	4*	−1.0*	3.24*
	14	5	−0.5	2.47	3	0.0	3.07	4*	−1.0*	3.24*

[a]The λ (unit in common logarithm) and Iteration represent Lagrange multiplier and iteration times at which the best RMS misfit was achieved, respectively. The * means manually determined model (see text).

We found that the Occam process occasionally failed. This occurred because an extremely small Lagrange multiplier gave rise to a large-contrast conductivity model, and thereby, an inversion process did not converge. In this case, we repeated the inversion with the Lagrange multiplier fixed at several values and determined the Lagrange multiplier and conductivity model that gave a minimal RMS misfit. This is represented as the manually determined model in Table 1, shown in the next section.

4. Results

Table 2 shows the RMS misfits that resulted from the various kinds of reference models (Table 1) and the default model covariance parameters, $4\tau\delta_i = 2.0$. No inversion attained stage II of the Occam process. The RMS misfit decreased as we incorporated more prior information into the reference model. In other words, the slab reference models provided smaller RMS misfits than any other layered or uniform reference model. The 5000 Ω m slab resistivity (model 12) diminished the RMS misfit by 0.18 compared to the 1000 Ω m resistivity (model 11), while an increase of slab resistivity to more than 5000 Ω m led to little improvement in RMS misfit. This result suggests that the gross resistivity of the subducting Pacific plate is at least 5000 Ω m in the shallow upper mantle below NEJ. We adopted the slab model with 5000 Ω m slab resistivity (model 12) as the best reference model. Figure 7 shows RMS misfit as a function of model covariance parameters, $4\tau\delta_i$, and the resultant Lagrange multiplier in terms of the best reference model. We determined the optimal $4\tau\delta_i$ to be 2.0, which gave the minimal RMS misfit. Table 1 shows the RMS misfits obtained by using the model covariance parameters of $4\tau\delta_i = 0.5$ and 8.0, respectively. Having carried out inversions in the wider model space, we could not find a superior model to the result of the best reference model and $4\tau\delta_i = 2.0$. Accordingly, we took the model obtained by using reference model 12 and $4\tau\delta_i = 2.0$ as the final result.

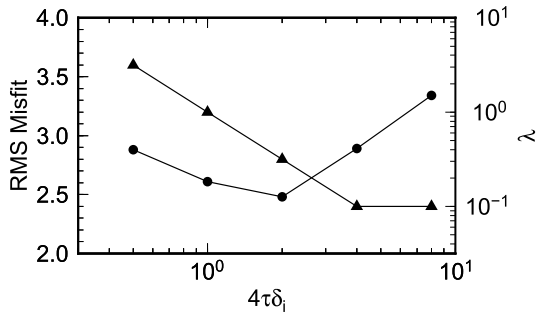

Figure 7. RMS misfit (circle) and Lagrange multiplier, λ, (triangle) as a function of model covariance parameter, $4\tau\delta i$, in terms of the best reference model (model 12 in Table 1).

Figure 8a shows map views of the resistivity distribution at the depths of 22.5, 32.5, 52.5, and 72.5 km. Figure 8b depicts them as resistivity perturbations relative to the reference model. Prominent conductive anomalies, C1 to C3, in the mid-crust (22.5 km) are observed beneath and in the vicinity of

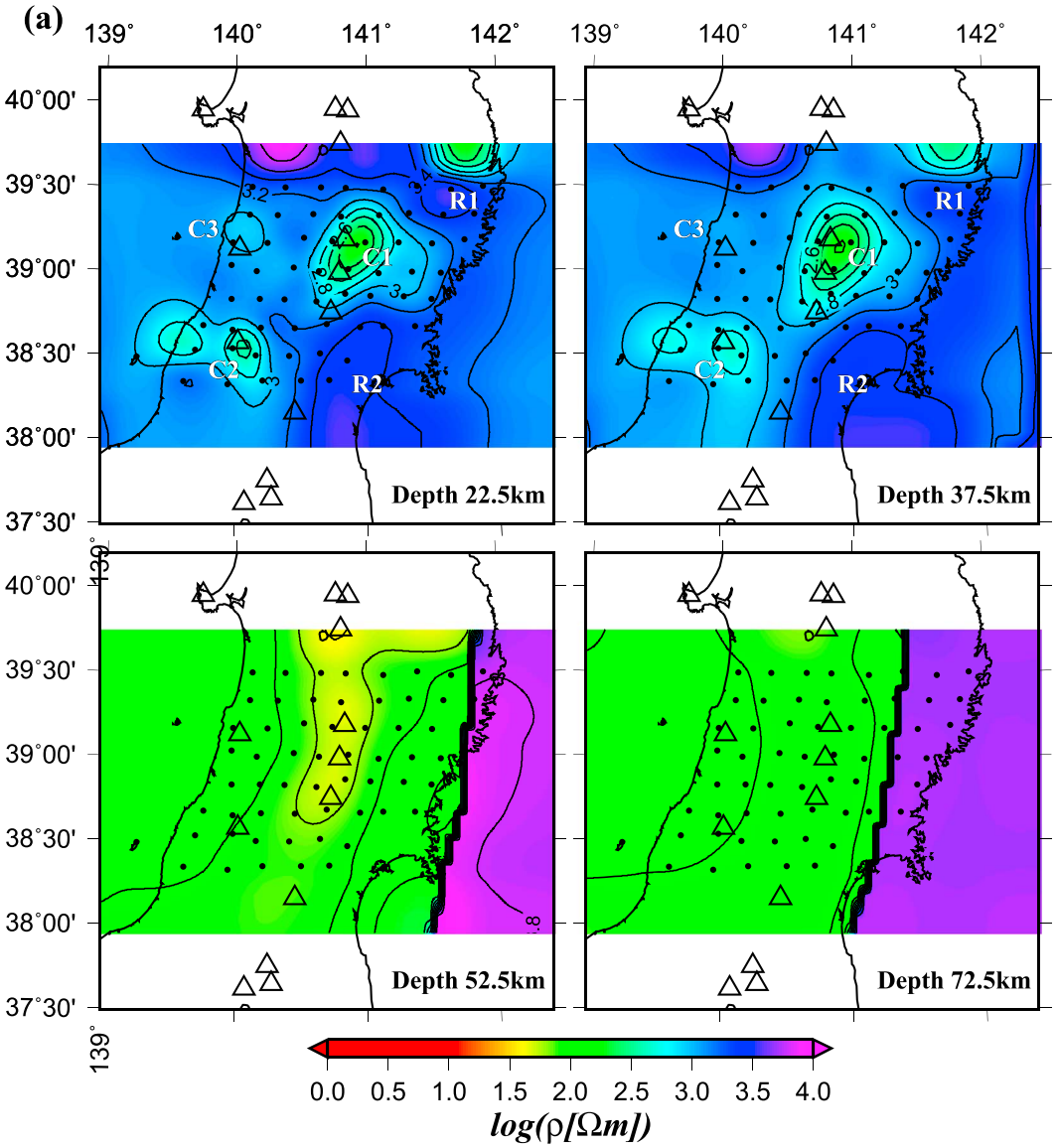

Figure 8. (a) Map views of resistivity distribution at depths of 22.5, 32.5, 52.5, and 72.5 km. C1 to C3 and R1 to R2 are prominent conductors and resistors discussed in text, respectively. Black dot and open triangle represent observation sites and volcanoes, respectively. (b) Same as Figure 8a but showing in the resistivity perturbation in terms of the best reference model (model 12 in Table 1).

Mts. Yakeishi, Gassan, and Chokai. The C1 and C2 conductors below Mt. Yakeishi and Mt. Gassan, respectively, extend to deeper levels, while the C3 conductor below Mt. Chokai disappears in the lower crust (32.5 km). The horizontal location of the C1 conductor follows OBR, whereas the C2 conductor retreats about 50 km to the back-arc side from OBR. These two aspects are clearly delineated in vertical profiles perpendicular to the trench axis (Figure 9). The B–B′ profile in Figure 9 runs through the C1 conductor below Mt. Yakeishi. The profile reveals that a conductive zone adhering to the subducting slab in the upper mantle detaches from the slab at a depth of 80–100 km and rises to the C1 conductor in the lower crust and uppermost mantle. On the other hand, the C–C′ profile passing through Mt. Gassan shows that the conductive zone rises toward the back-arc side after detaching from the slab. As a result, the conductive zone assumes the shape of an overturned plume, and the overturn likely gives rise to Mt. Gassan. The conductive zone adhering to the subducting slab at depths greater than 100 km is common to all the vertical profiles. Figure 9 also demonstrates that low-frequency earthquake swarms (represented by pink circles) occur in and around the C1 to C3 conductors in the lower crust and uppermost mantle, which is consistent with previous MT results targeting

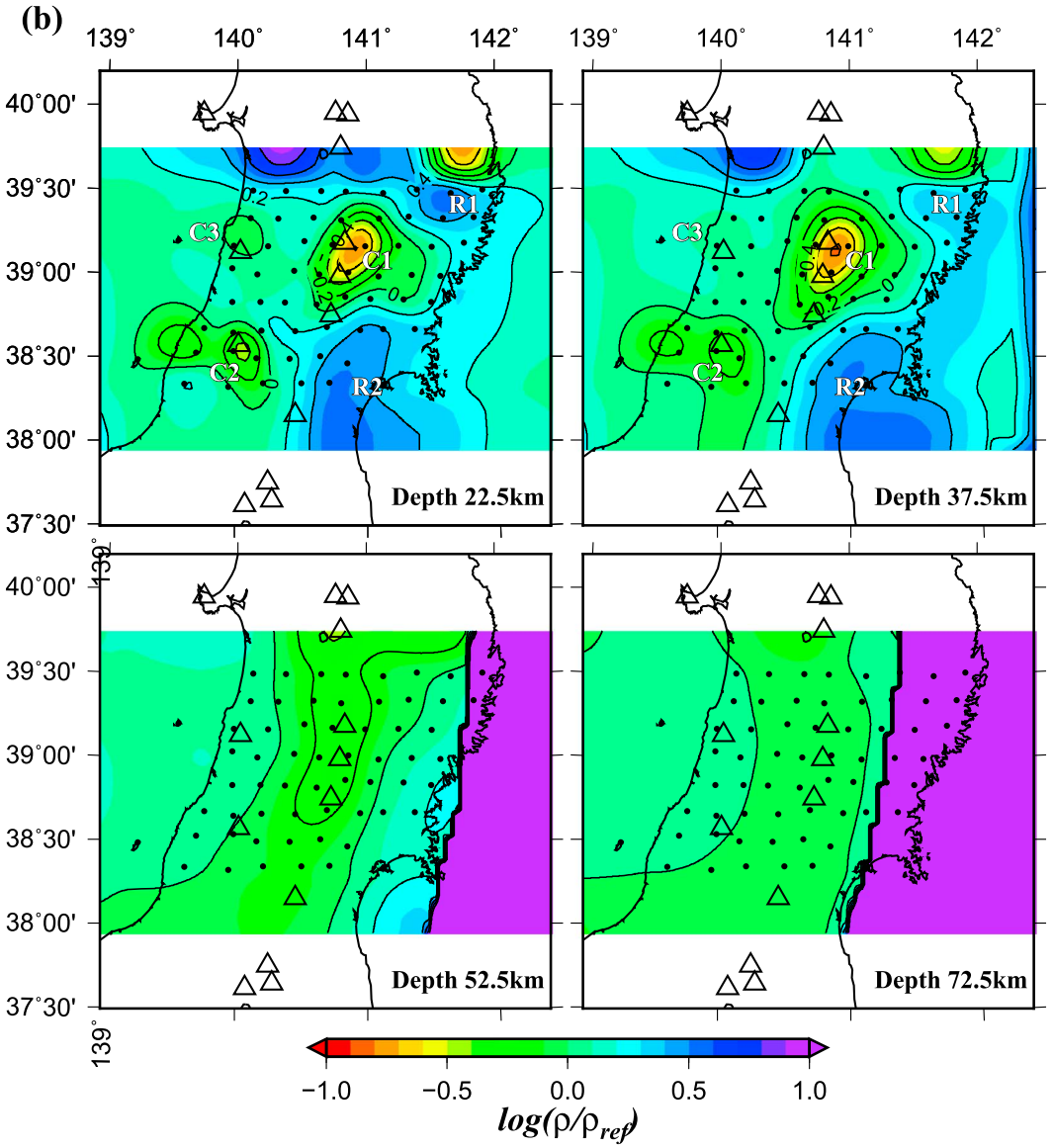

Figure 8. (continued)

the crust [e.g., *Mitsuhata et al*., 2001; *Ogawa et al*., 2001, 2014]. These low-frequency earthquake swarms are interpreted as volcanic or magmatic tremors because of their depths greater than the brittle-ductile transition zone and the nondouble-couple component of focal mechanisms [*Hasegawa and Yamamoto*, 1994]. We observed a couple of significant resistive anomalies, R1 and R2, in the crust below the fore arc. The R1 resistor is convincingly related to Tono batholiths, early Cretaceous granitic plutons in the Kitakami Mountains [*Tsuchiya and Kanisawa*, 1994, and references therein]: it is exposed at the earth's surface in the A–A′ profile, and the location of R1 in the map view at a depth of 22.5 km coincides with the surface distribution of Tono batholiths. The R2 resistor in profile C–C′ is not exposed at the earth's surface and has no correlation with surface geology. The presence of the R2 resistor is reliable, but in the next section, we demonstrate the limited resolution to the resistivity of this feature.

Figure 10a shows the spatial distribution of RMS misfit of the final model at eight periods. Each distribution is calculated from all four complex components of MT impedance tensor. The total RMS misfit is 2.48. The small RMS misfit at the period of 30,720 is due to the large standard errors. Although a few sites in the northeastern and southwestern marginal regions indicate poor RMS misfits throughout the period range, the final model accomplishes good spatially uniform fits of the data. Figure 10b shows the RMS distribution calculated from

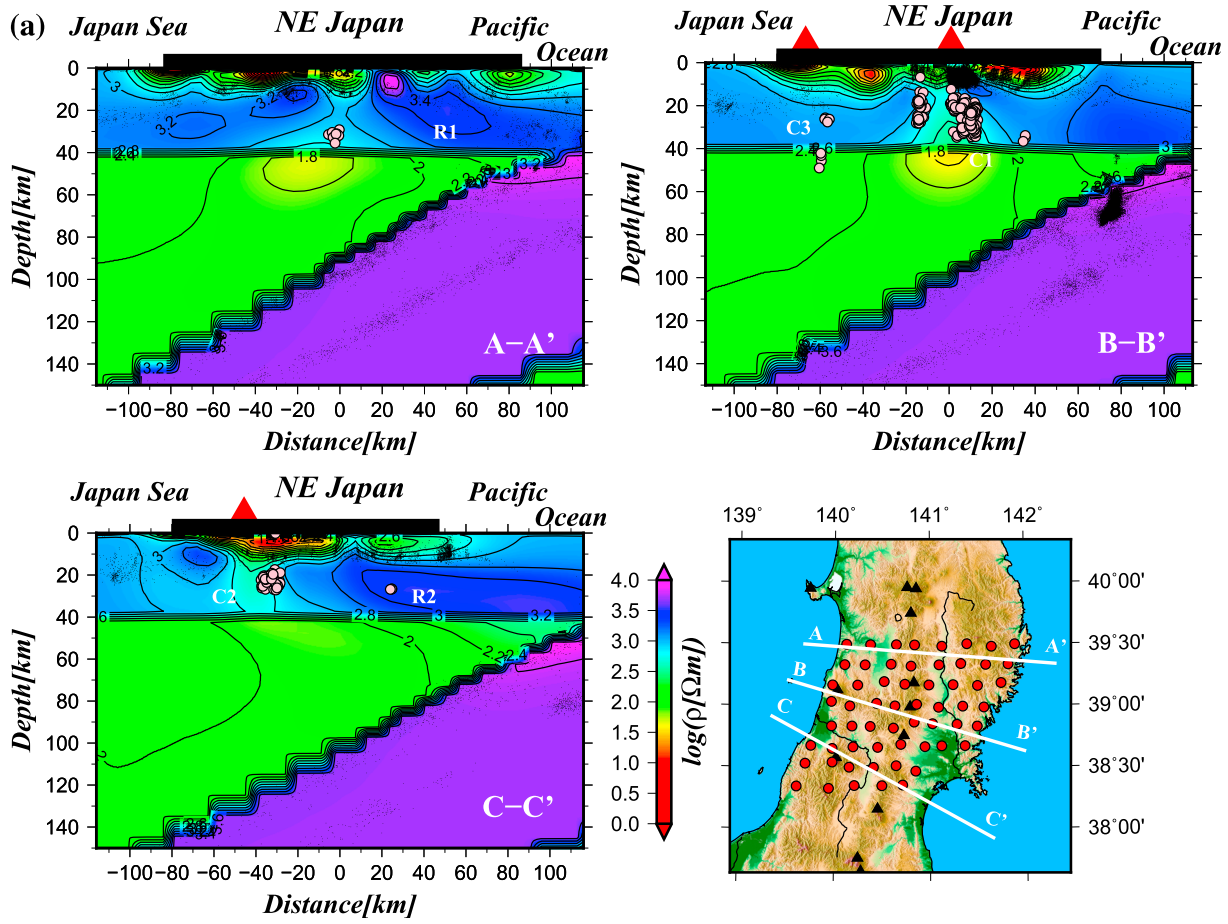

Figure 9. (a) Vertical profile of resistivity distribution perpendicular to the trench axis. Black dots and pink circles in resistivity profile represent normal microearthquakes and low-frequency tremors. Red triangles and thick horizontal solid lines show volcanoes and land area. C1 to C3 and R1 to R2 are prominent conductors and resistors discussed in text, respectively. (b) Same as Figure 9a but showing in the resistivity perturbation in terms of the best reference model.

the 3-D model obtained by using reference model 6. The total RMS misfit is 2.72. The reference model 6 does not contain a slab. An improvement in RMS misfit (Figure 10a) is found in the region surrounding the yellow line at periods of 960 and 1920 s. Incorporating the subducting slab into the reference model results in the inclusion of an intricate mantle wedge toe into the model. This improves the RMS misfits over the mantle wedge toe region at periods of 960 and 1920 s.

So far, we have not mentioned the geomagnetic transfer function. Because of the limitation of our computer resources and calculation time, geomagnetic transfer function data were not used simultaneously in the inversion. In this paper, we only compared the observed induction arrows with those calculated from the final resistivity model. The observed and calculated induction arrows at periods of 320, 1920, 5120, and 15,360 s are shown in the supporting information. The observed and calculated induction arrows fit fairly well, although the fits of induction arrows as well as magnetotellurics at a period of 15,360 s are poor.

5. Sensitivity Test for Key Features

To test the sensitivity and resolvability of key features in the obtained electrical conductivity model, we derived a modified Fréchet derivative calculation and a boxcar test simulating the pseudo-impulse response of the inversion process. The key features treated here are (1) the C1 conductor near the Moho below Mt. Yakeishi, (2) the R2 resistor below the fore arc, (3) the C2 conductor and the overturn of the

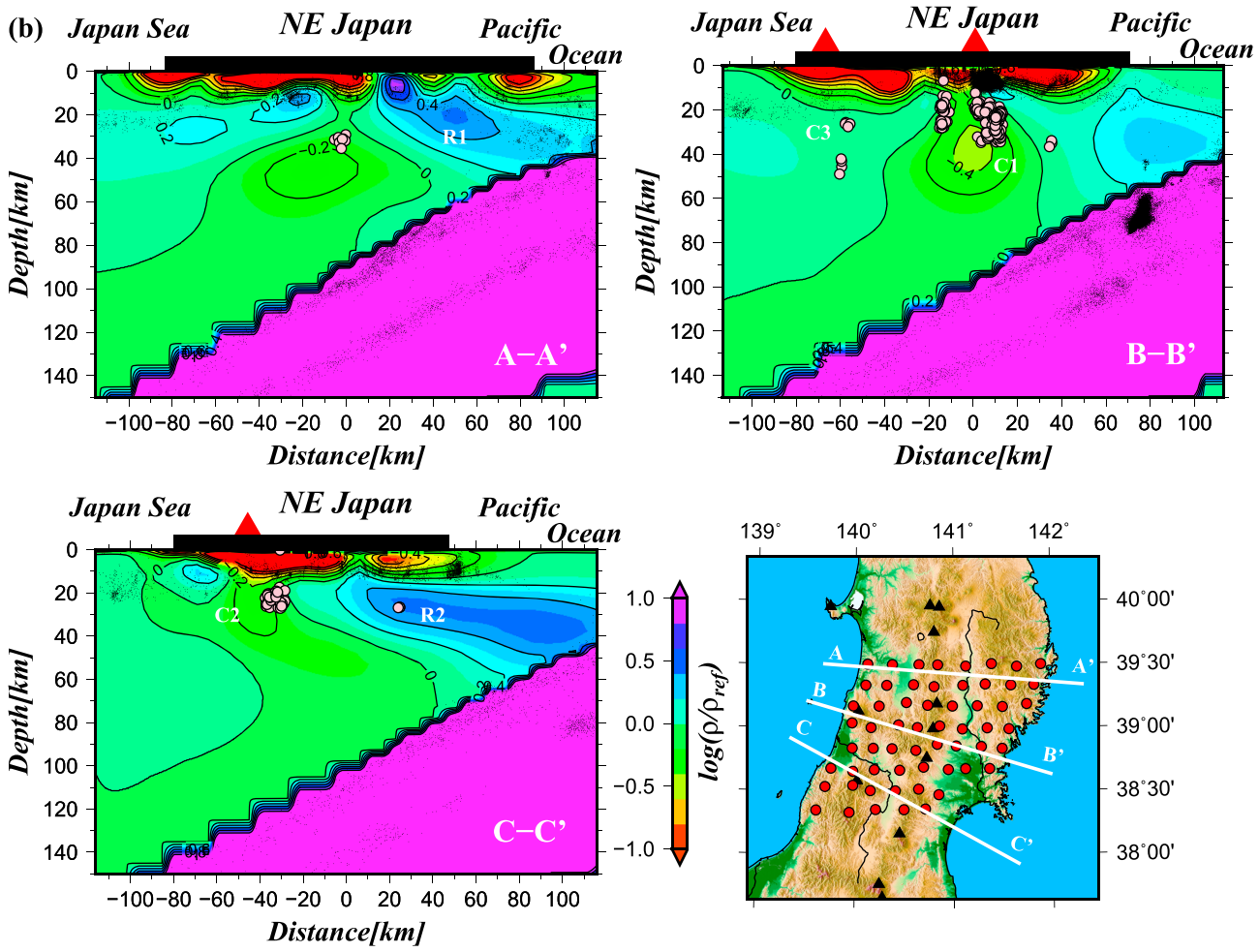

Figure 9. (continued)

conductive body on profile C–C′, and (4) the conductive zone adhering to the subducting slab at depths greater than 100 km.

Fréchet derivative permits the calculation of a locally linearized change in response due to a change in a reference model [e.g., *Boerner and West*, 1989]. In magnetotellurics, the Fréchet derivative is defined as

$$\delta Z_{ij}(\mathbf{r}_k, \mathbf{x}, T) = \int K_{ij}(\mathbf{r}_k, \mathbf{r}', \mathbf{m}, T)\delta\mathbf{m}(\mathbf{r}')d\mathbf{r}' + O\left(\|\delta\mathbf{m}(\mathbf{r}')\|^2\right), \quad (2)$$

where K_{ij} is the Fréchet derivative ($i, j = x, y$ components). Other parameters are Z_{ij}: MT impedance, $\mathbf{r}_k$: the location vector of each observation station k, $\mathbf{r}'$: the location of the perturbed model parameter, $\mathbf{x}$: a certain representative location of the perturbed region ($\mathbf{x} \in \mathbf{r}'$), $\mathbf{m}$: a model parameter as a function of space, and T: the period. Next, we treat the summation of the above equation in terms of the observation station (hereafter denoted as Δ_{ij}):

$$\Delta_{ij}(\mathbf{x}, T) = \sum_{k}^{\text{sites}} \int K_{ij}(\mathbf{r}_k, \mathbf{r}', \sigma_0(\mathbf{r}'), T)\delta\log\rho(\mathbf{r}')d\mathbf{r}', \quad (3)$$

where ρ and σ_0 indicate resistivity and reference conductivity, respectively. We took the perturbation of logarithmic resistivity as $\delta\mathbf{m}(\mathbf{r}')$. In the one-dimensional case, *Oldenburg* [1979] derived the following analytical form of equation (2):

$$\delta Z(T) = \int \mu_0\sigma_0(z)\left(\frac{E(z,T)}{B(0,T)}\right)^2 \delta\ln\rho(z)dz, \quad (4)$$

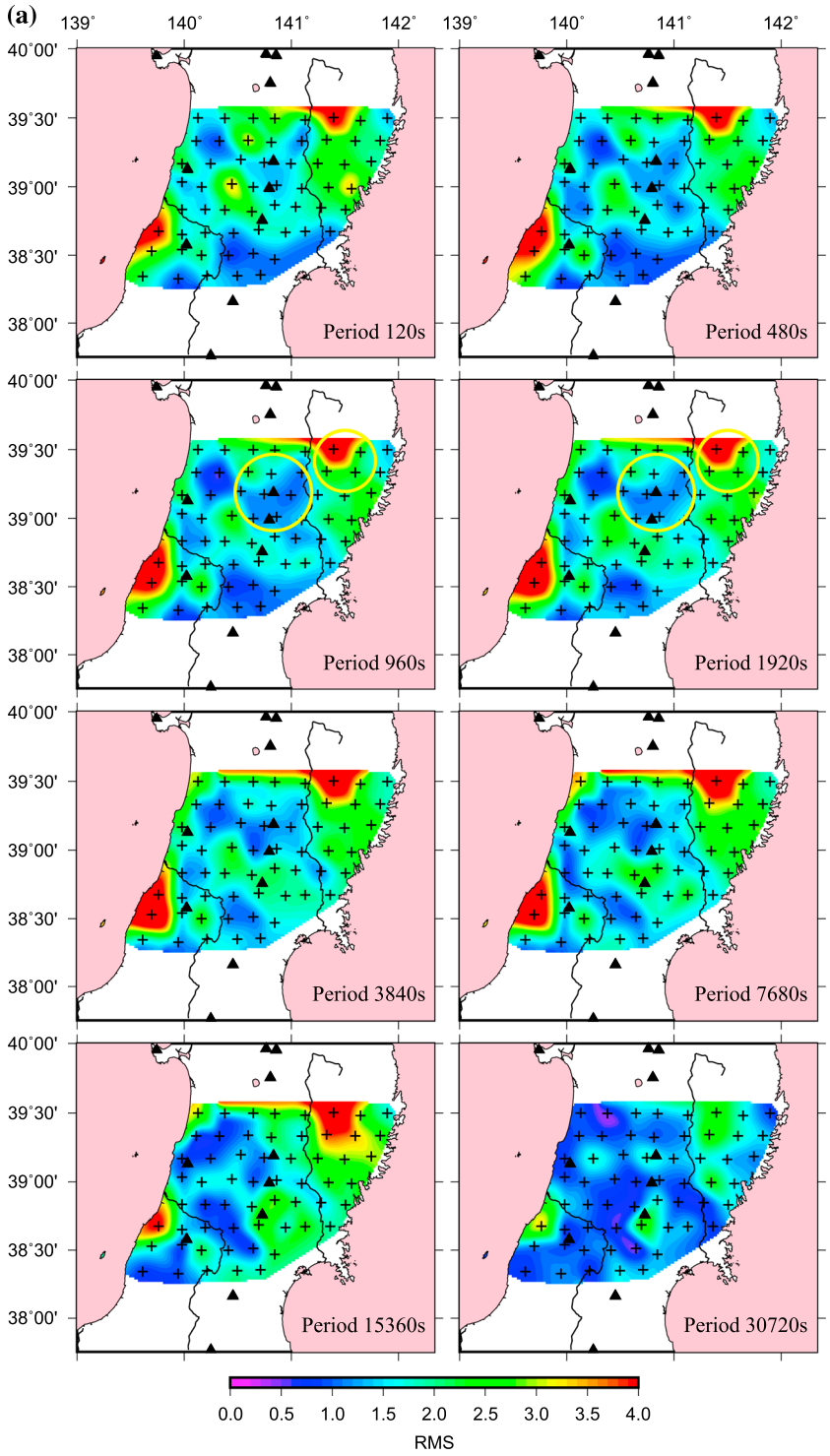

Figure 10. (a) Spatial distribution of RMS misfit at eight periods in terms of the final model (obtained by using reference model 12 and $4\tau\delta_i = 2.0$). Cross and close triangle show observation site and volcano, respectively. Yellow circles represent the areas in which RMS misfits are significantly improved by using the reference model 12 incorporating the subducting slab into. (b) Spatial distribution of RMS misfits of the 3-D model obtained by using reference model 6 and $4\tau\delta_i = 2.0$. The reference model 6 is a slab-free model from reference model 12. RMS misfits in the area as shown by yellow circles are inferior to those in Figure 10a. See text for details.

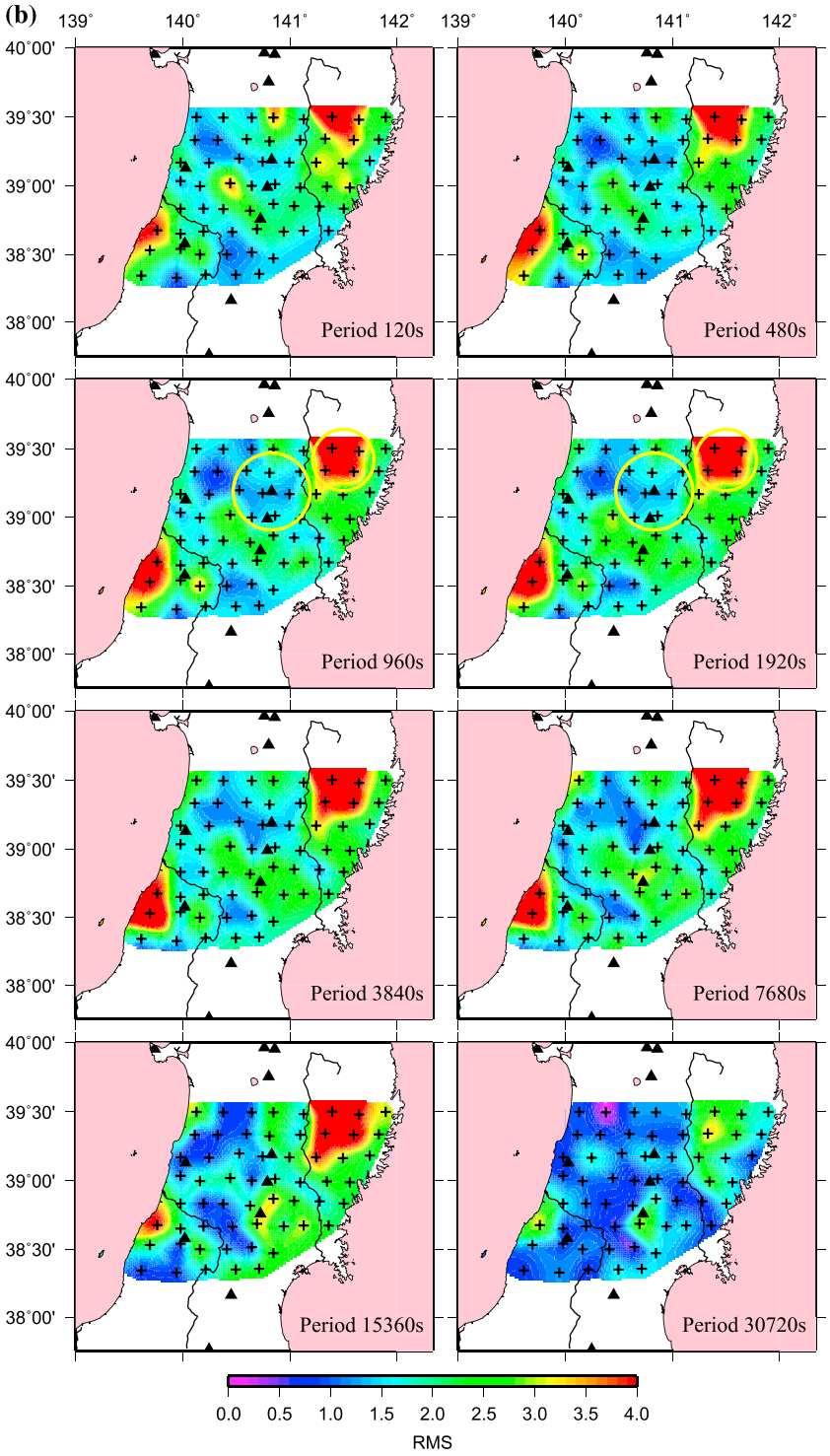

Figure 10. (continued)

where $E(z,T)$ and $B(0,T)$ are the electric field at depth z and magnetic flux density at the earth's surface, respectively. If we assume that the 3-D Fréchet derivative takes a form similar to that of the one-dimensional case, equation (3) is reduced to

$$\Delta_{ij}(\mathbf{x}, T) = \mu_0 \sigma_0(\mathbf{x}) \delta \log \rho(\mathbf{x}) \delta V(\mathbf{x}) \sum_{k}^{\text{sites}} \kappa_{ij}(\mathbf{r}_k, \mathbf{x}, T), \tag{5}$$

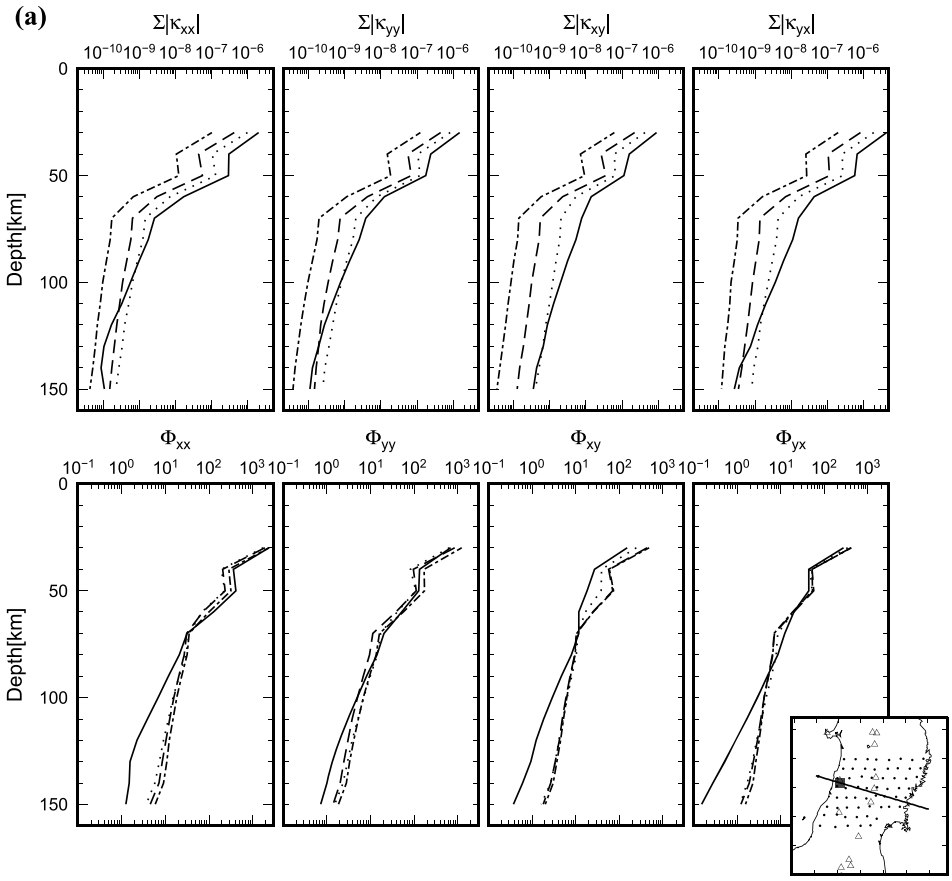

Figure 11. (top) Total modified Fréchet derivative and (bottom) upper bound of total phase change as a function of depth below (a) back arc, (b) Ou Backbone Range, and (c) fore arc, at the periods of 60 (solid line), 480 (dotted line), 3840 (dashed line), and 30,720 (chain line) s, respectively. Vertical axis corresponds to the depth of the center of perturbed cube. Unit of total modified Fréchet derivative is $\Omega^2\,m^{-2}\log^{-2}$ (S/m). The perturbed cube of 20 km on side is located along B–B′ profile, and the assigned resistivity perturbation is three orders of magnitude more conductive than the best reference model. Locations of B–B′ profile (solid line) and perturbed cubes (shaded areas) are shown in each child map in the plain view.

where $\mathbf{x}$ is a representative location of perturbed region $\mathbf{r}'$. In equation (5), we assumed the following conditions to simplify the expression: (1) the perturbed region $\mathbf{r}'$ is comparatively small and (2) $K_{ij}[\mathbf{r}_k,\mathbf{r}',\sigma_0(\mathbf{r}'),T]$, σ_0, and $\delta\log\rho$ are constant within the perturbed region, respectively. $\sum_k^{\text{sites}}\kappa_{ij}(\mathbf{r}_k,\mathbf{x},T)$ indicates the relative sensitivity in terms of perturbed location $\mathbf{x}$ on the condition of observation network, $\mathbf{r}_k$. We hereafter call this the total modified Fréchet derivative (TMFD). We do not divide TMFD by the number of sites to discuss the resolvability of the observation network—when the MT response change is locally restricted in an observation network, the average is affected by the number of insensitive observation sites. If we compare a resolvability of an observation network to that of a narrower one with a same observation density, the average operation results in an unfair evaluation of the wider observation network. In the following forward calculation for estimating TMFD, we allotted -2.0 and an approximate cube with length on a side of 20 km to $\delta\log\rho(\mathbf{x})$ (two orders of magnitude more conductive) and the perturbed region, respectively. Note that we obtained almost the same results using the resistivity contrast -1.0. To display the final TMFD, we show the summation of absolute amplitude, viz. $\sum_k^{\text{sites}}\left|\kappa_{ij}(\mathbf{r}_k,\mathbf{x},T)\right|$. The TMFD provides a kind of amplitude response sensitivity. To delineate phase response sensitivity, we show the upper bound on the total phase change in terms of observation sites. The phase change at each site, $\delta\varphi_{ij}(\mathbf{r}_k,\mathbf{x},T)$, is expressed as

$$\delta\varphi_{ij}(\mathbf{r}_k,\mathbf{x},T)\precsim\frac{\left|\delta Z_{ij}(\mathbf{r}_k,\mathbf{x},T)\right|}{\left|Z_{ij}(\mathbf{r}_k,\mathbf{x},T)\right|} \tag{6}$$

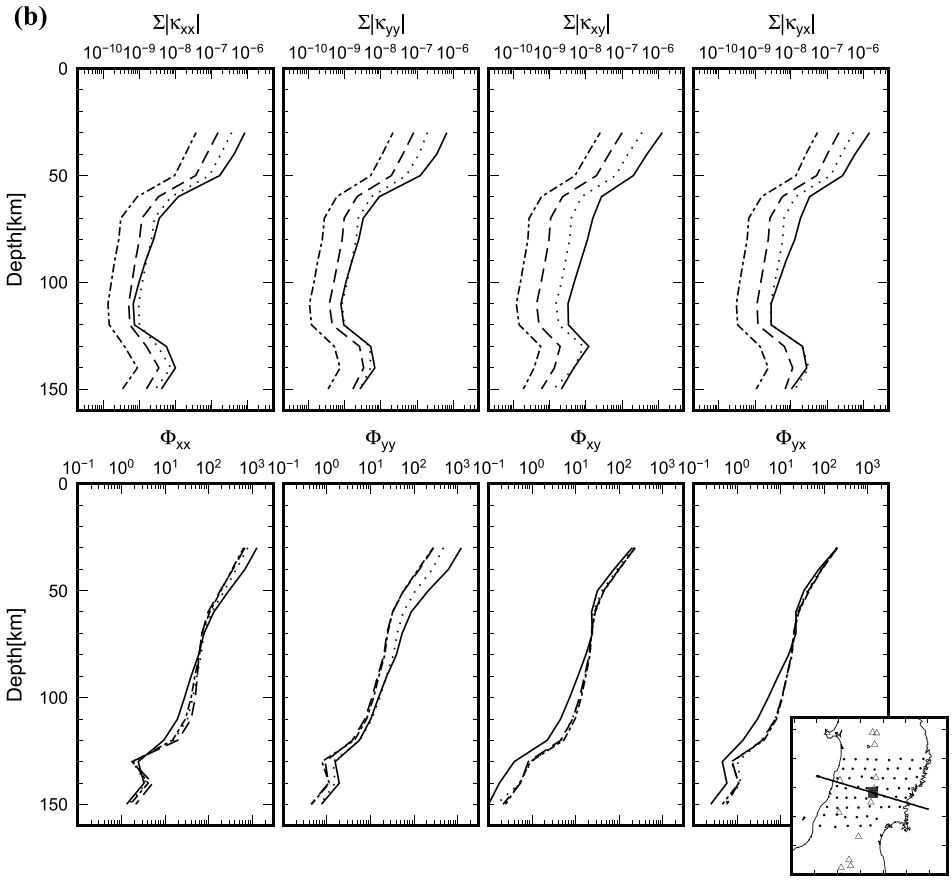

Figure 11. (continued)

and the upper bound on the total phase change, $\Phi_{ij}(\mathbf{x},T)$, is

$$\Phi_{ij}(\mathbf{x},T) = \sum_{k}^{\text{sites}} \frac{\left|\delta Z_{ij}(\mathbf{r}_k,\mathbf{x},T)\right|}{\left|Z_{ij}(\mathbf{r}_k,T)\right|}, \tag{7}$$

where $Z_{ij}(\mathbf{r}_k,T)$ in equations (6) and (7) is the impedance response at site k and period T to the reference model.

The TMFD and $\Phi_{ij}(\mathbf{x},T)$ down to 150 km below the back arc, OBR, and fore arc in the B–B′ profile are plotted in Figure 11. The site locations are identical to those for the real data, and the reference model is fixed on the best reference model (model 12 in Table 1). The TMFD deeper than 100 km below back arc is an order of magnitude smaller than that at 50 km depth and about two orders of magnitude less than that of the crust, respectively. The $\Phi_{ij}(\mathbf{x},T)$ of each component deeper than 100 km below the back arc is less than 10°. These results suggest that feature (4) is poorly resolved with our MT data. On the other hand, the TMFD and $\Phi_{ij}(\mathbf{x},T)$ of the entire period range have sufficient sensitivity down to 40 km below the back arc, OBR, and fore arc. Hence, the C1 conductor is well constrained by our MT data. With regard to feature (3), the lateral sensitivity contrast in profile C–C′ is important, as is the sensitivity at crustal depths. If the lateral sensitivity contrast of the crust is significant in the C–C′ profile, the C2 conductor might actually be located in an insensitive region in the crust and uppermost mantle, which could cause the overturn image in profile C–C′ to disappear. In other words, if the location below OBR has a poor sensitivity in profile C–C′ and the C2 conductor relocates below OBR, the overturn image would immediately vanish. Figure 12 shows the lateral sensitivity contrast of the crust in profile C–C′. To estimate Figure 12, we allocated a 10 Ω m cube with sides of 20 km to between 20 and 40 km depth and moved the cube laterally along profile C–C′. Our MT site distribution provides the best sensitivity at the C2 conductor location in profile C–C′.

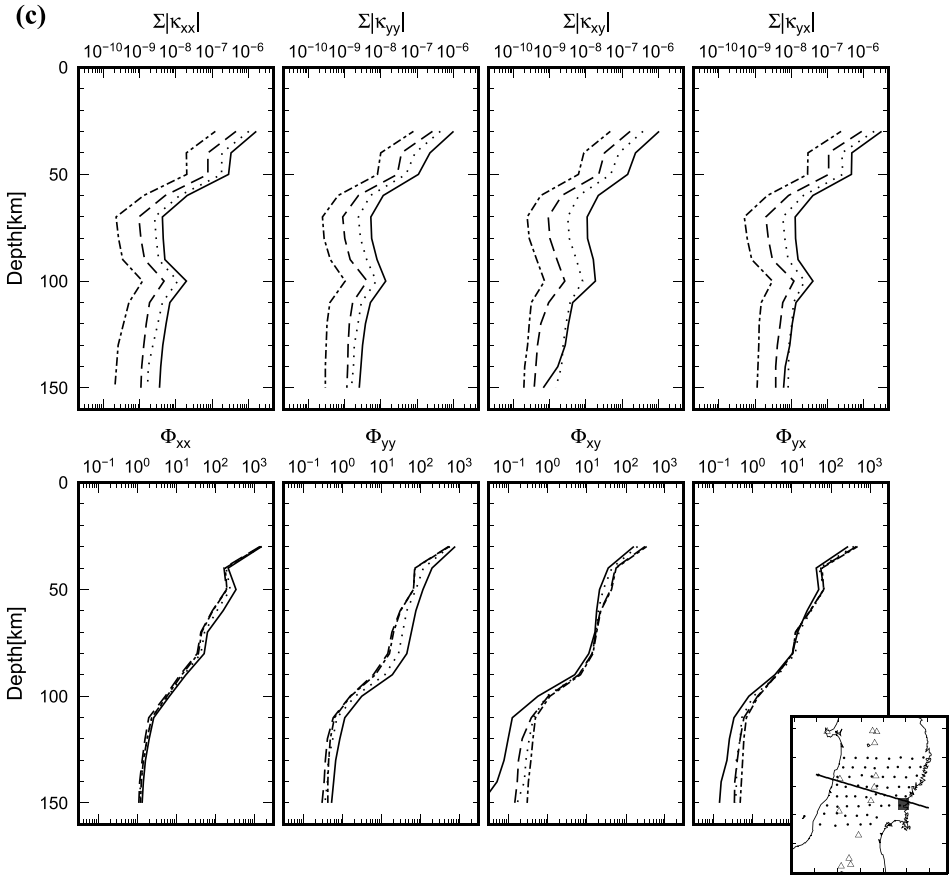

Figure 11. (continued)

For example, the Φ_{yy}[**x**(C2),60*s*] is at most one order of magnitude greater than the least sensitive region. This strongly suggests that the C2 conductor below the back arc in profile C–C′ is a required feature. However, the TMFD and Φ_{ij}(**x**,*T*) diminish below OBR because of the lack of observation sites, and the conductive region could expand to the low resolution region below OBR. Assuming that the conductive region expands below OBR, the conductor in the C–C′ profile may be a funnel shape rather than an overturn shape. To clarify this conductive image, we estimated the TMFD and Φ_{ij}(**x**,*T*) in another profile (Z–Z′) across the C2 conductor between the depths of 20 and 40 km (Figure 13). The TMFD and Φ_{ij}(**x**,*T*) in Z–Z′ show almost the same lateral sensitivity. None of the conductive bodies in the crust below OBR and fore arc is imaged, and the conductive region also shows the overturn in Z–Z′. As a result, the middle to lower crust in the eastern vicinity of the C2 conductor is not as conductive as C2, and the conductive overturn shape is convincingly delineated with our MT data.

The boxcar test is used to reinvert synthetic data calculated from a model in which a conductive or resistive cube is embedded in a certain reference model. The reinverted model indicates a kind of impulse response of the inversion process in terms of the reference model, and it allows us to evaluate how much the resistivity image obtained by the inversion blurs and the bias of the resistivity contrast. In other words, the inversion process always outputs more or less blurred (smoothing) image than an actual contrast. The boxcar test gives the degree of the blurring. We checked the resolution of the C1 conductor and the R2 resistor in Figures 8 and 9 by use of this boxcar test. The reference model and site location are the same as for the Fréchet derivative calculation, and the employed periods of synthetic data are identical to the 12 used in the inversion. To make the synthetic data for the C1 conductor and R2 resistor, we embedded a 1 Ω m (three orders of magnitude conductive) and a 100 k Ω m (20 factors of magnitude resistive) cube with sides of 20 km into the reference model, respectively (Figure 14). We appended Gaussian random noise with a 5% standard deviation to the synthetic impedance data. The Lagrange multiplier ($10^{-0.5}$) and model

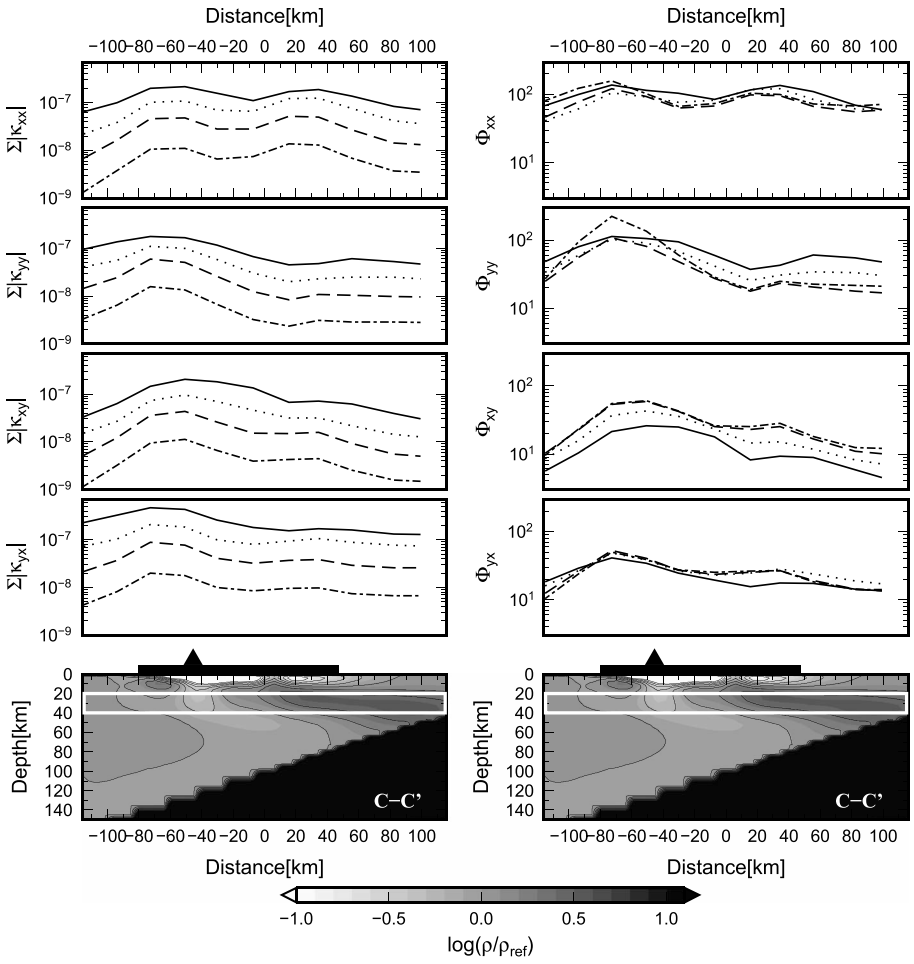

Figure 12. Total modified Fréchet derivative and upper bound of total phase change as a function of lateral location along C–C′ profile. Solid, dotted, dashed, and chain line represents the results at periods of 60, 480, 3840, and 30,720 s, respectively. The resistivity perturbation is embedded in 20 to 40 km depth in C–C′ profile as is shown by white rectangles in the bottom figures. Thick line and triangle represent location of land and volcanoes.

covariance parameters ($4\tau\delta_i = 2.0$) were fixed at those of the final model in section 4. The vertical profile of the reinverted model is shown in Figure 14 for comparison with the input model. The number of iterations of each inversion was one, and the RMS misfit fell below 1.0. Because of the fixed Lagrange multiplier, stage II of the Occam process was not performed. In the boxcar test for the C1 conductor, the outline of the conductive region is almost comparable to that of the C1 conductor in Figure 9. The recovered conductive region greater than 0.2 orders of magnitude assumes a width as large as 40 km. The recovered conductivity contrast is only up to 0.6 orders of magnitude more conductive than the reference model despite the three orders of magnitude conductivity contrast in the input model. This boxcar test reveals that the absolute resistivity obtained in this method is definitely biased toward resistive values. Indeed, the resistivity of the C1 conductor obtained with the inversion (ca. 800 Ω m) is considerably more resistive compared with lower crustal conductors seen in previous studies [e.g., *Ogawa et al*., 2001, 2014; *Mishina*, 2009; *Ichihara et al*., 2014]. Figure 15 shows another boxcar test for the C1 conductor using 1, 10, and 100 Ω m cubes with the same volume. The recovered conductive regions using 1 and 10 Ω m cube has a similar volume and resistivity contrast with that of the C1 conductor in profile B–B′, while the result of 100 Ω m cube obviously shows a weak contrast resistivity image. Consequently, the actual volume of the C1 conductor is comparable with that of a cube with sides of 20 km, but the resistivity is about 10 Ω m or more conductive. The boxcar test for the R2 resistor resulted in complete disappearance of the resistive block

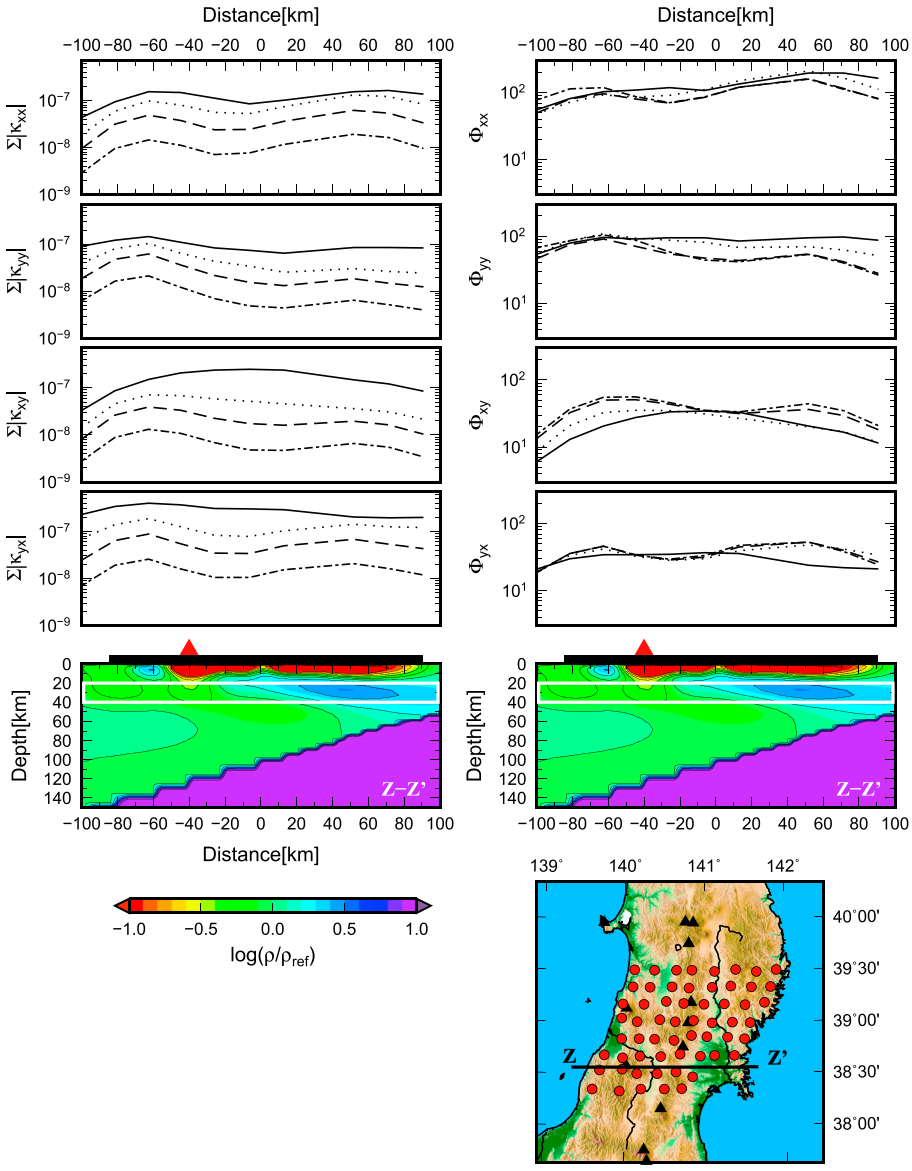

Figure 13. Same as Figure 12 but along Z–Z′ line as is shown in the inset child map. Z–Z′ line is in east-west direction.

(Figure 14). The absence of an observation site above the R2 resistor as well as the boxcar test suggests that the R2 resistor is poorly resolved.

6. Discussion

Our 3-D electrical resistivity model contains the following important features: (1) A conductive body has an overturned-plume shape in profile C–C′, with the conductive plume head reaching the lower crust beneath the back-arc volcano Mt. Gassan. (2) The most prominent lower crust and uppermost mantle conductors occur below Mt. Yakeishi on OBR. The resistivity of the conductive body in the lower crust is less than 10 Ω m, and the volume is comparable to that of a 20 km cube on a side. The conductor is continuous from the lower crust to the subducting slab surface. We next discuss the tectonic implications and geophysical significance of these key features.

6.1. Overturn of Electrically Conductive Plume and Back-Arc Volcanism

Back-arc volcanism in NEJ has been interpreted as resulting from a mantle diapir originating from the subducting slab at a depth of 150–200 km [e.g., *Hasegawa and Nakajima*, 2004]. Petrological studies have suggested that

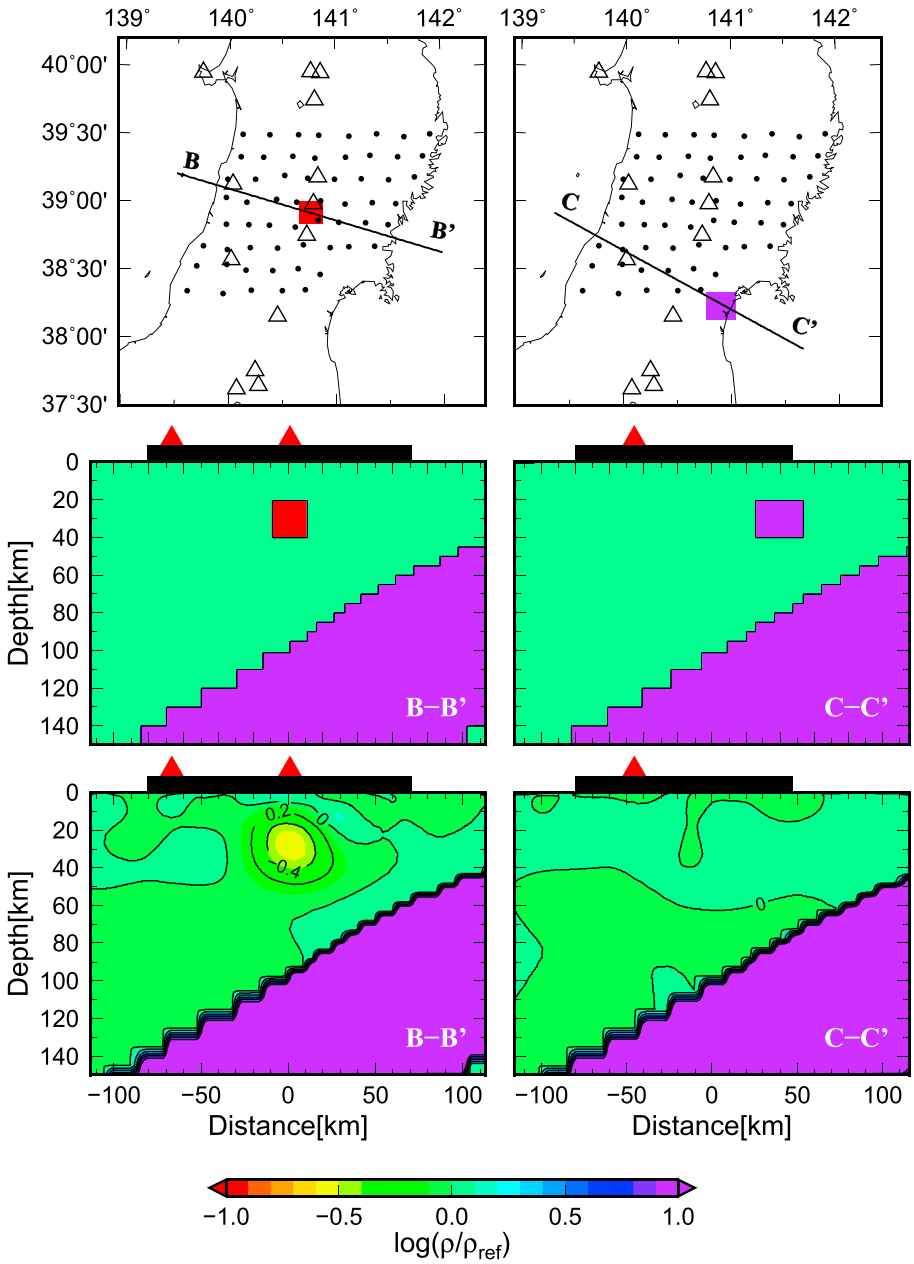

Figure 14. Boxcar test for (left) C1 conductor in B–B′ vertical profile and for (right) R2 resistor in C–C′ profile. Upper (map view) and middle (vertical view) figures are input models with conductive or resistive cube. The lower figure is a recovered model in vertical view.

dehydration of phlogopite [*Tatsumi*, 1989], phengite, and lawsonite [*Pawley*, 1994; *Poli and Schmidt*, 1995] could yield such a mantle diapir below the back-arc region. A numerical study also demonstrated the onset of the mantle diapir separating from the subducting slab at 150–200 km depth [*Gerya and Yuen*, 2003]. Hence, we had expected a conductor isolated in the upper mantle beneath the back arc. However, our electrical resistivity model revealed no such conductor isolated in the shallow upper mantle beneath the back arc. In contrast, the model profile in C–C′ (Figure 9) delineates a conductive plume overturned toward the back-arc direction, the head of which reaches the lower crust below Mt. Gassan. This indicates that fluids released from the subducting slab at depths of 80–100 km move upward toward the back-arc direction and that overturning of the fluids yields the back-arc volcanism. The conductive plume at 40 to 80 km depth shows a weak resistivity contrast in the model. As we demonstrated in the previous section, this resistivity would be biased toward the resistive values.

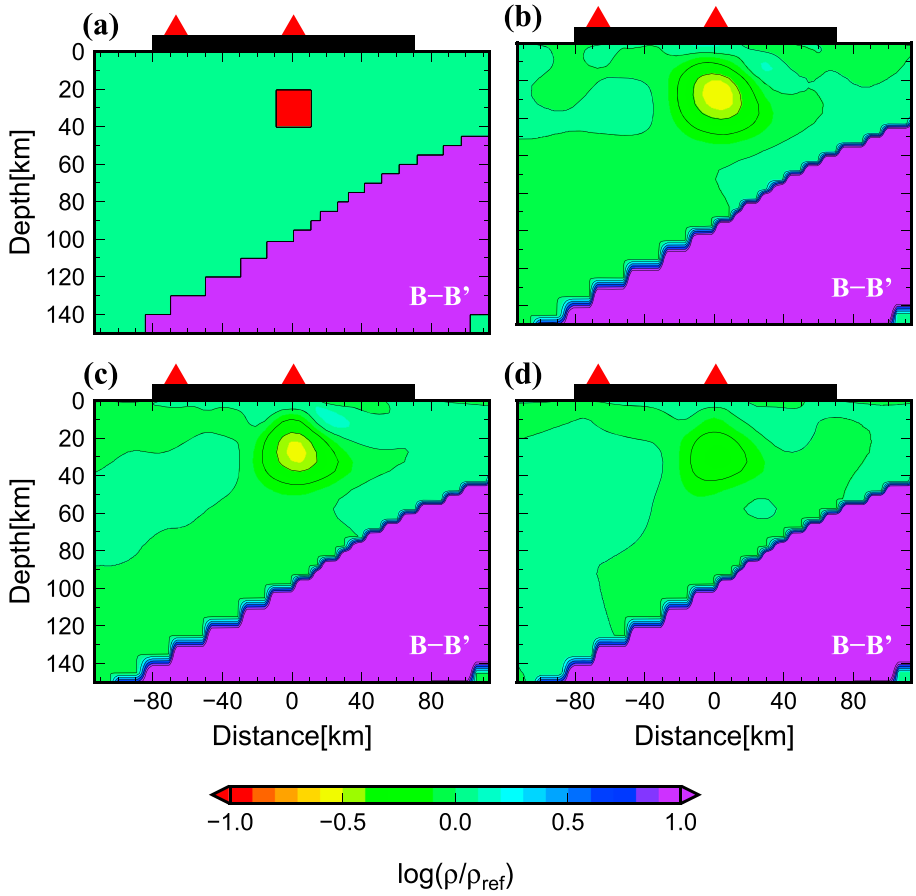

Figure 15. Boxcar test for C1 conductor resistivity. (a) The input model composed of the cube with 20 km on side in vertical view. The 1, 10, and 100 Ω m is allotted to the resistivity of the cube, respectively. The recovered model calculated from 1, 10, and 100 Ω m cube is shown in Figures 15b–15d, respectively, in vertical view.

The consequential issue is what enables the overturning of the upwelling fluids in the mantle wedge. *Currie and Hyndman* [2006] advocated a conceptual model in which small-scale (ca. 100 km wavelength) poloidal convections in the trench-perpendicular direction were depicted [see Figure 16 proposed by *Currie and Hyndman*, 2006]. The small-scale poloidal convections are derived from thermal convections. We have interpreted that the overturn in our model corresponds to lateral flow in the across-arc direction from upwelling toward the downflow of the thermal convections. A numerical study of subduction zone dynamics realized such an overturn in the mantle wedge [*Davies and Stevenson*, 1992, denoted as DS92 hereafter]. DS92 employs a two-dimensional Stokes flow formulation with the Boussinesq approximation. When a buoyant body with a buoyancy number greater than 10^6 emerges in the mantle wedge close to a subducting slab, the buoyant body assumes an overturned shape (described as flow reversal by DS92). The buoyancy number is defined as $gd^3\Delta\rho/(\kappa\eta)$, where d: the specific length of the buoyant body, $\Delta\rho$: density perturbation, g: gravity acceleration, κ: thermal diffusivity, and η: viscosity. DS92 estimated 2 wt. % water content and 1130–1180°C temperature of melt to account for 10^6 of buoyancy number. Using these parameters, a laboratory experiment of peridotite melt conductivity yielded 0.9–2.0 S/m [*Ni et al.*, 2011]. If we assume that the resistivity of the mantle wedge conductive zone is comparable to the C1 and C2 conductors (viz. less than 10 Ω m in resistivity as is shown in section 5), this estimation is consistent with our model. Note that conductivity with 100% melt fraction should be used in the argument above because of Stokes flow condition. Volcanism on the hot finger track from Mt. Chokai to Mt. Kurikoma has migrated 70–80 km eastward in the last 5 Ma [*Kondo et al.*, 2004]. This eastward migration of volcanism might result from suppression of the overturning of upwelling fluid/melt owing to a reduction of the buoyancy number of the upwelling fluid/melt. Honda and his colleagues represented the hot fingers as a result of roll-like convection

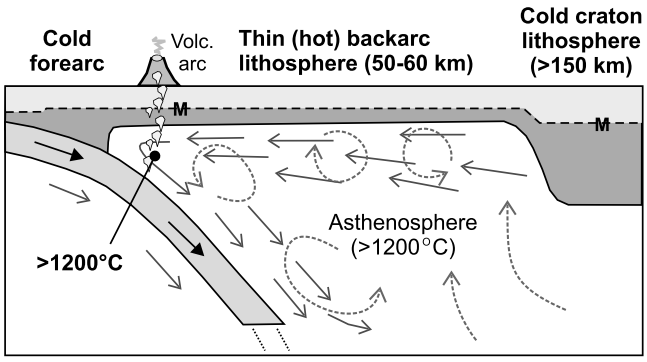

Figure 16. Conceptual model of mantle wedge flow proposed by *Currie and Hyndman* [2006]. A slab subducts from the upper left to the lower right in this figure. Solid and dashed arrows indicate the viscous coupling of slab and thermal convection, respectively.

or Rayleigh-Taylor instability [*Honda and Saito*, 2003; *Zhu et al*., 2009], i.e., a two-dimensional and along-arc poloidal convection image. On the other hand, the overturn in our resistivity model indicates that there are small-scale poloidal convections in the across-arc direction. These two aspects suggest that the mantle wedge flow below NEJ assumes Rayleigh-Bénard convection rather than Rayleigh-Taylor instability and that the overturn in our model corresponds to the lateral flow in the across-arc direction from upwelling to downflow of Bénard cells. *Currie and Hyndman* [2006] cited short horizontal wavelength (about 100 km) seismic velocity variation in the western United States as evidence [*Gao et al*., 2004; *Yang and Forsyth*, 2006] to advocate the presence of small-scale convections in the mantle wedge. Recent high-resolution electrical resistivity [*Meqbel et al*., 2014] and seismic velocity studies [*Schmandt and Humphreys*, 2010; *Gilbert et al*., 2012; *Tian and Zhao*, 2012; *Jones et al*., 2014] have revealed undulations of resistivity and seismic velocity distribution at the Moho and lithosphere-asthenosphere boundary in the western United States. Those results indicate the presence of Bénard cells beneath the back arc. The distance between C2 and C3 is about 70 km, which is comparable to the wavelength of the seismic velocity and resistivity variations in the western United States.

Allowing for upwelling of partial melt or infiltration of melt into grain boundaries or cracks, we should consider the porous flow governed by Darcy's law [*McKenzie*, 1984; *Katz et al*., 2007; *Cagnioncle et al*., 2007; *Wilson et al*., 2014] rather than the Stokes flow. However, it has yet to be studied whether numerical simulation allowing for the porous flow can cause the overturned flow in the mantle wedge and under which condition the overturn can occur. Here we consider the porous flow in the mantle wedge assuming the permeability distribution model proposed by *Wada et al*. [2011]. They modeled grain size distribution in the mantle wedge and converted the grain size distribution into a permeability distribution by using the Blake-Kozeny-Carman equation [*Bear*, 1972]. The permeability distribution has a similar pattern to the overturn configuration. When fluid/melt emerges in a mantle wedge with this permeability distribution calculated by *Wada et al*. [2011], Darcy's law tells us that fluid/melt moves up toward the back arc (see supporting information). Thus, the porous flow could cause the overturned flow. However, this heterogeneous permeability cannot explain the vertical conductive body below OBR (profiles A–A′ and B–B′).

Although the overturn of the conductive body is not prominent below Mt. Chokai (or the C3 conductor) in profile B–B′, the overturn likely takes place in the middle crust in this profile. Seismic tomography studies in NEJ [e.g., *Huang et al*., 2011; *Nakajima et al*., 2001] show that positive *Vp* and *Vs* perturbations at 40 km depth below the back-arc region of our profile B–B′ decrease abruptly to negative perturbations at 25 km depth. Moreover, their vertical seismic wave velocity profiles evidently delineate the overturn image of slow seismic wave velocity perturbation in the middle crust below the back arc in our profile B–B′ location. *Hasegawa et al*. [2008] depicted an overturn image of slow *Vs* on a vertical profile passing the northern vicinity of Mt. Chokai in the across-arc direction. The inflection point of the slow *Vs* overturn is as deep as 20 km, which is consistent with our resistivity model. Seismic wave velocity and resistivity images seem to corroborate the presence of overturn of fluid/melt toward the back-arc direction in the middle crust.

6.2. On the Lower Crust Conductor

6.2.1. Quantitative Interpretation of the Lower Crust Resistivity

The most distinctive conductive body, C1, is observed at depths of 20 to 50 km below OBR in profile B–B′. The boxcar test in section 5 suggests that the resistivity of C1 is less than 10 Ω m. We calculated the volume fraction of fluid/melt by which a resistivity less than 10 Ω m in the lower crust can be explained. In the calculation,

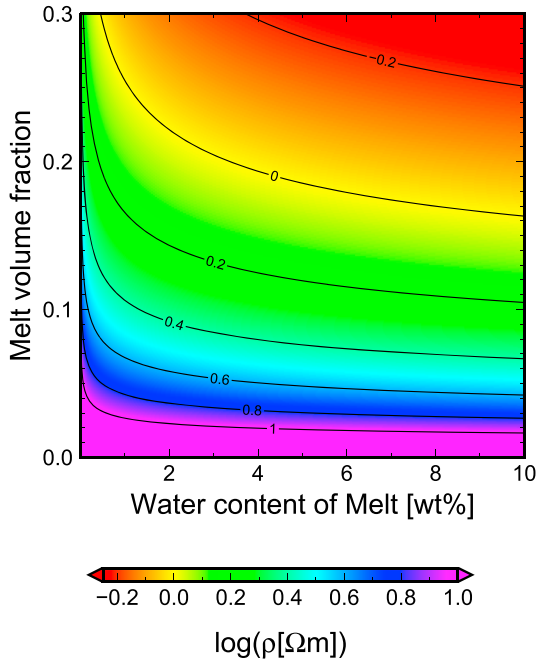

Figure 17. Bulk resistivity of the composites of amphibolite and hydrous melt at 1 GPa in pressure and 800°C in temperature. Hydrous melt resistivity depends on melt water content. Contour line unit is in log(Ω m). The amphibolite and melt conductivity data are from *Fuji-ta et al.* [2011] and *Gaillard* [2004], respectively. Hashin-Shtrikman upper bound is used to calculate bulk resistivity.

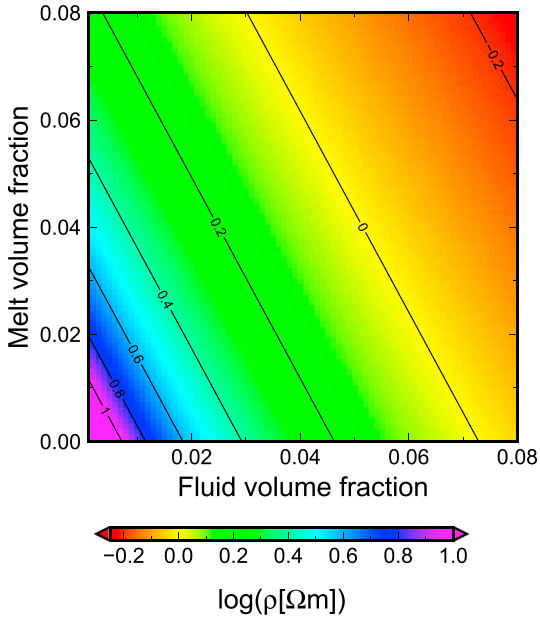

Figure 18. Bulk resistivity of the composites of amphibolite, water-saturated melt, and aqueous sodium chloride with 17 wt. % at 1 GPa in pressure and 800°C in temperature. Conductivity of aqueous sodium chloride with 17 wt. % is from *Shimojuku et al.* [2014]. Other data and representation are the same with Figure 17.

we used 1 GPa and 800°C of pressure and temperature, respectively. The mantle xenoliths sampled at Ichinomegata indicate that the equilibrated temperature in the uppermost mantle is about 800°C [*Takahashi*, 1980, 1986]. Because the water-saturated solidus of felsic and mafic rocks at 1 GPa is 600–700°C [e.g., *Wolf and Wyllie*, 1994, and references therein], melt could be present in the lower crust. Melt conductivity in the lower crust, σ_{melt}, is calculated from the equation for amphibolite (obsidian) melt obtained by *Gaillard* [2004]:

$$\sigma_{melt} = \sigma_0 \exp[(-E_a + 20P)/(RT)] \quad (8)$$

$$\sigma_0 = -78.9 \ln(W) + 754 \quad (9)$$

$$E_a = -2925 \ln(W) + 64132 \quad (10)$$

where P is pressure in MPa, T is temperature in Kelvin, R is the gas constant in J mole^{-1} K^{-1}, and W is the water content in wt. % (note that Gaillard's original paper contains a typographical omission). The conductivity of amphibolite is

$$\sigma_{solid} = \sigma_0 \exp[-E_a/(kT)], \quad (11)$$

where $\sigma_0 = 0.8385$ S/m, $E_a = 0.4874$ eV, and k is the Boltzman constant in eV/K. The data are from BC-3 shown by *Fuji-ta et al.* [2011; *Fuji-ta*, personal communication]. The Hashin-Shtrikman upper bound [*Hashin and Shtrikman*, 1962] is used to calculate bulk resistivity.

We consider two cases. The first is that all saline fluid dissolves in melt, and the bulk configuration is composed of lower crustal rock and melt. Figure 17 shows the relation between volume fraction of melt and bulk resistivity of the melt-rock composite. The melt fraction needed to account for the 10 Ω m in bulk resistivity is 1.5 vol. %. This estimate is consistent with 1–2 vol. % at 40 km depth of fluid/melt calculated from the seismological data [*Nakajima et al.*, 2005]. A 2 vol. % (upper bound) melt/fluid fraction derived from seismological data corresponds to a resistivity in the lower crust of 7–8 Ω m. The second case is the coexistence of melt and saline fluid. That is, melt is saturated with water

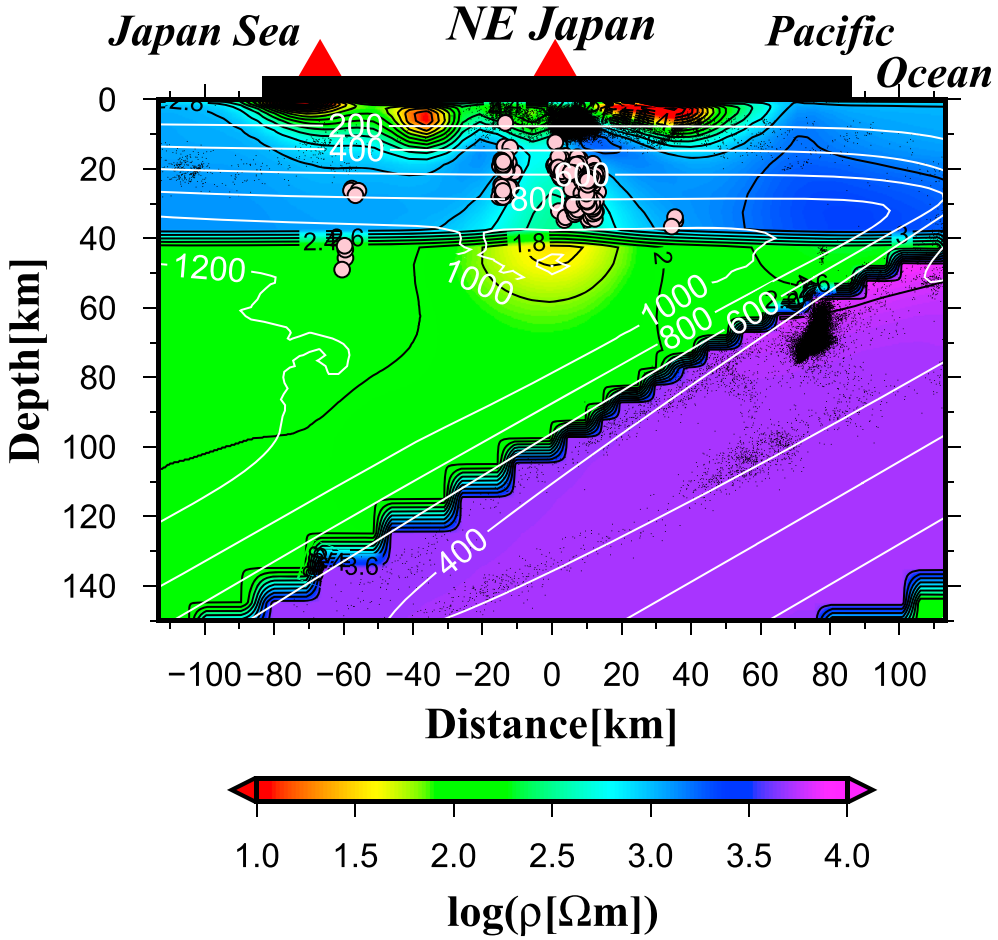

Figure 19. Thermal model beneath NEJ by *Iwamori* [2007] superimposed on the resistivity profile in B–B′. White line shows isotherms. Unit is in °C. Slab surface temperature at 100 km depth is about 600°C and is much cooler than Cascadia. See text for detail.

and excess water exists as saline fluid. The solubility of water in rhyolitic melts is 10 wt. % using the equation of *Tamic et al.* [2001]. The conductivity of melt with 10 wt. % water content is 8.658 S/m. Fluid inclusions [e.g., *Roedder*, 1984], fluids dehydrated from the subducting slab [e.g., *Manning*, 2004], and fluids sampled in the deep crust [e.g., *Bucher and Stober*, 2010] are all predominantly composed of aqueous sodium chloride and calcium chloride solutions. Because calcium cation mobility is negligible [*Gaillard*, 2004; *Shimojuku et al.*, 2014], the major charge carriers in aqueous fluid and melt under lower crustal conditions are sodium and chloride ions. Thus, we assume that the saline fluid is aqueous sodium chloride solution. For simplicity, we do not allow for the partition coefficients of sodium and chlorine between melt and saline fluid phases, but rather employ the conductivity of saline fluids estimated by *Shimojuku et al.* [2014]. Figure 18 shows the bulk resistivity of water-saturated melt, saline fluid with 17 wt. % salinity (20 S/m), and amphibolite. The Hashin-Shtrikman upper bound for multiple phases is reduced to

$$\sigma_{\text{bulk}} = \sigma_1 + A/[1 - A/(3\sigma_1)] \tag{12}$$

$$A = \sum_{i=2}^{N} \frac{f_i}{1/(\sigma_i - \sigma_1) + 1/(3\sigma_1)}, \tag{13}$$

where $\sigma_1 > \ldots > \sigma_i > \sigma_{i+1} > \ldots > \sigma_N$. σ_{bulk} is the bulk conductivity and f_i is the volume fraction of i's medium [*Park and Ducea*, 2003]. The end member of the second case is that melt volume is approximately zero. In this case, the total amount of fluid/melt fraction is also a minimum. To account for 10 Ω m in the lower crust, only 0.7 vol. % of fluid/melt is required. For consistency with the upper bound volume fraction estimated by the seismic data (2 vol. %), the lower crustal conductor would need to be more than 0.3 Ω m.

6.2.2. Fluid Transport Pathway From Slab Surface to Lower Crust

The conductive zone extends from the lower crust conductor to the slab surface at 80–100 km depth below OBR. This indicates that the fluid/melt pathway, that is, fluid accompanying the subducting slab is "segregated" from the slab at 80–100 km depth and rises to the lower crust conductor below OBR.

Because our resistivity model has insufficient resolution in the mantle wedge deeper than 100 km, the model can neither resolve the depth down to which the conductive zone extends nor determine the source location of fluid/melt. Based on a 2-D model of Cascadia, *McGary et al.* [2014] revealed a fluid/melt pathway similar with that in profile B–B′ of our model. They interpreted that the primary source existed at the slab surface at about 100 km depth. However, this interpretation cannot be adapted to the subduction zone beneath NEJ because the age of the subducting plate beneath Cascadia (up to 10 Ma) is much younger than that beneath NEJ (about 130 Ma at the trench). The temperature at the slab surface at 100 km depth is as low as 600°C beneath NEJ [*Iwamori*, 1998, 2007], which is much cooler than the 1150°C of the Cascadia geothermal setting (see Figure 19). According to seismic tomography [e.g., *Zhao et al.*, 1992; *Nakajima et al.*, 2001], laboratory experiments [e.g., *Iwamori*, 1998, 2007; *Schmidt and Poli*, 1998], and ocean bottom magnetotellurics [*Toh et al.*, 2006], the dehydration of dragged hydrous peridotite and of subducting MORB beneath NEJ likely takes place at depths as deep as 150 to 200 km. The connection between the dehydration field at 150 to 200 km depth and the segregation of fluid/melt at 80–100 km depth remain unresolved because of low resolution below 100 km depth in our model. The resistivity contrast of the plume at 40 to 80 km depth is weak (60–100 Ω m in the final model). However, this resistivity would be biased toward the resistive values, as we demonstrated in the boxcar test.

As it reached the lower crust, the fluid/melt remains in the lower crust. This feature is consistently observed in subduction zones of the world [South America: *Brasse and Eydam*, 2008; North America: *Patro and Egbert*, 2008; *Rippe et al.*, 2013; *McGary et al.*, 2014; *Meqbel et al.*, 2014; New Zealand: *Heise et al.*, 2007; *Wannamaker et al.*, 2009; see also *Shankland and Ander*, 1983]. The reason why fluid/melt remains in the lower crust and uppermost mantle is possibly due to the formation of impermeable cap layers owing to increasing dihedral angle and/or silica precipitation in the saline fluid. The dihedral angle hypothesis has been proposed by many researchers [e.g., *Hyndman and Shearer*, 1989]. Indeed, laboratory experiments have revealed that the dihedral angle in anorthite aggregates with aqueous fluid was more than 60° below 1 GPa pressure, whereas it decreased below 60° with increasing pressure [*Yoshino et al.*, 2002]. Silica precipitation also contributes to interrupting the rise of fluid/melt in the crust. Such silica precipitation is probably stimulated as saline fluid rises to the middle or upper crust because silica solubility in saline fluid decreases with the exchange of concomitant solute cation from sodium to calcium [*Shumlovich et al.*, 2006]. The exchange of solute cation could take place when saline fluid rises to the middle or upper crust with lithological facies change. Furthermore, silica solubility in saline fluid essentially decreases as pressure and temperature diminish [e.g., *Manning*, 1994].

The location of the C1 conductor is below Mts. Yakeishi and Kurikoma and the hypocentral region of the 2008 Iwate-Miyagi Nairiku Earthquake (M 7.2) [e.g., *Okada et al.*, 2010, 2012, 2014]. Three isolated conductive bodies (less than 10 Ω m in resistivity and 10 to 20 km in width and depth) were observed in this region by *Ichihara et al.* [2014] and *Ogawa et al.* [2014]. The C1 conductor of our study corresponds to the merger of two conductors below Mts. Yakeishi and Kurikoma.

7. Conclusion

Our 3-D model of the subduction zone below NEJ contains a vertically continuous conductive body from the lower crust to the slab surface below Mts. Yakeishi and Kurikoma on OBR. The conductive body indicates a fluid/melt pathway from the slab surface to lower crust. The lower crust conductor is 10 Ω m or more conductive in resistivity. The 0.7 vol. % at minimum of fluid/melt is required to account for 10 Ω m resistivity in the lower crust, and the resistivity of the lower crust conductor greater than 0.3 Ω m is in agreement with the 1 to 2 vol. % of fluid/melt volume fraction derived from seismological data [*Nakajima et al.*, 2005].

Other resistivity profiles in the across-arc direction show that the conductive body segregates from the subducting slab at 80–100 km depth and takes an overturned form toward the back-arc direction. The head of the conducting body reaches the lower crust just below Mt. Gassan, which is one of the prominent back-arc volcanoes. Hence, the back-arc volcanism is likely not caused by a mantle diapir but rather by fluid/melt overturn rising toward the back-arc direction. A numerical simulation with Stokes flow formulation

showed that the overturn or flow reverse toward the back arc takes place in the case of a buoyancy number greater than 10^6 [*Davies and Stevenson*, 1992]. The conductive overturn distribution indicates the presence of small-scale poloidal convections in the across-arc direction. Allowing for the presence of poloidal convections in the along-arc direction as well as those in the across-arc direction, the mantle wedge flow below NEJ likely assumes Rayleigh-Bénard convection rather than Rayleigh-Taylor instability.

Acknowledgments

Hiroshi Ichihara (Japan Agency for Marine-Earth Science and Technology), Hiromi Fukino, Izumi Sato, and Oliver Hartkorn (Tokyo Institute of Technology), Sadato Ueki, Yasuo Yabe, Takuro Iida, and Keisuke Yoshida (Tohoku University), and Nobutaka Hozumi (Kyoto University) helped greatly with the fieldwork. Special thanks are extended to Eiichi Takahashi (Tokyo Institute of Technology) for his continuous encouragement. Kiyoshi Fuji-ta (Osaka University) kindly allowed us to show the result of the laboratory experiments. Hikaru Iwamori (Japan Agency for Marine-Earth Science and Technology), Junichi Nakajima, Tomomi Okada, Toru Matsuzawa, and Michihiko Nakamura (Tohoku University), and Hiroshi Sakuma (National Institute for Materials Science) provided us with fruitful discussions. Magnetotelluric equipments with the gimballed system were provided by the University of Tokyo. The Geomagnetic Chart in 2010 used in this paper is available at Geospatial Authority of Japan. We used seismic hypocenter location data determined by the Japan Meteorological Agency, the National Research Institute for Earth Science and Disaster Prevention, the Geoinformation Authority of Japan, Hokkaido University, Hirosaki University, Tohoku University, the University of Tokyo, Nagoya University, Kyoto University, Kochi University, Kyushu University, Kagoshima University, Japan Agency for Marine-Earth Science and Technology, the National Institute of Advanced Industrial Science and Technology, the Tokyo Metropolitan Government, the Aomori Prefectural Government, the Shizuoka Prefectural Government, the Hot Springs Research Institute of Kanagawa Prefecture, and Yokohama City. We partly carried out the numerical calculation using the computer systems of the Earthquake and Volcano Information Center of the Earthquake Research Institute, the University of Tokyo, and the TSUBAME computer service, Tokyo Institute of Technology. Alan Chave (Woods Hole Oceanographic Institution) kindly provided the bounded influence remote reference processing code. Most parts of the figures were created with the Generic Mapping Tool [*Wessel and Smith*, 1998]. Constructive comments by the associate editor and two anonymous reviewers greatly improved the manuscript. This work was supported financially by the Japan Society for the Promotion of Science KAKENHI, 21109003, 20403006, 23403004, and 26109006.

References

Aizawa, K., et al. (2014), Three-dimensional resistivity structure and magma plumbing system of the Kirishima Volcanoes as inferred from broadband magnetotelluric data, *J. Geophys. Res. Solid Earth*, *119*, 198–215, doi:10.1002/2013JB010682.

Bear, J. (1972), *Dynamics of Fluids in Porous Media*, 764 pp., American Elsevier Publ. Com., New York.

Bibby, H. M., T. G. Caldwell, and C. Brown (2005), Determinable and non-determinable parameters of galvanic distortion in magnetotellurics, *Geophys. J. Int.*, *163*, 915–930, doi:10.1111/j.1365-246X.2005.02779.x.

Boerner, D., and G. F. West (1989), Fréchet derivatives and single scattering theory, *Geophys. J. Int.*, *98*, 385–390, doi:10.1111/j.1365-246X.1989.tb03359.x.

Brasse, H., and D. Eydam (2008), Electrical conductivity beneath the Bolivian Orocline and its relation to subduction processes at the South American continental margin, *J. Geophys. Res.*, *113*, B07109, doi:10.1029/2007JB005142.

Bucher, K., and I. Stober (2010), Fluids in the upper continental crust, *Geofluids*, *10*, 241–253, doi:10.1111/j.1468-8123.2010.00279.x.

Cagnioncle, A.-M., E. M. Parmentier, and L. T. Elkins-Tanton (2007), Effect of solid flow above a subducting slab on water distribution and melting at convergent plate boundaries, *J. Geophys. Res.*, *112*, B09402, doi:10.1029/2007JB004934.

Caldwell, T. G., H. M. Bibby, and C. Brown (2004), The magnetotelluric phase tensor, *Geophys. J. Int.*, *158*, 457–469, doi:10.1111/j.1365-246X.2004.02281.x.

Chave, A. D., and D. J. Thomson (2004), Bounded influence magnetotelluric response function estimation, *Geophys. J. Int.*, *157*, 988–1006, doi:10.1111/j.1365-246X.2004.02203.x.

Constable, S. C., R. L. Parker, and C. G. Constable (1987), Occam's inversion: A practical algorithm for generating smooth models from electromagnetic sounding data, *Geophysics*, *52*, 289–300, doi:10.1190/1.1442303.

Cruciani, C., E. Carminati, and C. Doglioni (2005), Slab dip vs. lithosphere age: No direct function, *Earth Planet. Sci. Lett.*, *238*, 298–310, doi:10.1016/j.epsl.2005.07.025.

Currie, C. A., and R. D. Hyndman (2006), The thermal structure of subduction zone back arcs, *J. Geophys. Res.*, *111*, B08404, doi:10.1029/2005JB004024.

Davies, J. H., and D. J. Stevenson (1992), Physical model of source region of subduction zone volcanics, *J. Geophys. Res.*, *97*, 2037–2070, doi:10.1029/91JB02571.

DeMets, C., R. G. Gordon, and D. F. Argus (2010), Geologically current plate motions, *Geophys. J. Int.*, *181*, 1–80, doi:10.1111/j.1365-246X.2009.04491.x.

Fuji-ta, K., T. Katsura, M. Ichiki, T. Matsuzaki, and T. Kobayashi (2011), Variations in electrical conductivity of rocks above metamorphic conditions, *Tectonophysics*, *504*, 116–121, doi:10.1016/j.tecto.2011.03.008.

Gaillard, F. (2004), Laboratory measurements of electrical conductivity of hydrous and dry silicic melts under pressure, *Earth Planet. Sci. Lett.*, *218*, 215–228, doi:10.1016/S0012-821X(03)00639-3.

Gao, W., S. P. Grand, W. S. Baldridge, D. Wilson, M. West, J. F. Ni, and R. Aster (2004), Upper mantle convection beneath the central Rio Grande rift imaged by *P* and *S* wave tomography, *J. Geophys. Res.*, *109*, B03305, doi:10.1029/2003JB002743.

Gerya, T. V., and D. A. Yuen (2003), Rayleigh-Taylor instabilities from hydration and melting propel 'cold plumes' at subduction zones, *Earth Planet. Sci. Lett.*, *212*, 47–62, doi:10.1016/S0012-821X(03)00265-6.

Gilbert, H., Y. Yang, D. W. Forsyth, C. H. Jones, T. J. Owens, G. Zandt, and J. C. Stachnik (2012), Imaging lithospheric foundering in the structure of the Sierra Nevada, *Geosphere*, *8*, 1310–1330, doi:10.1130/GES00790.1.

Green, D. H. (1973), Experimental melting studies on a model upper mantle composition at high pressure under water-saturated and water-undersaturated conditions, *Earth Planet. Sci. Lett.*, *19*, 37–53, doi:10.1016/0012-821X(73)90176-3.

Hasegawa, A., and A. Yamamoto (1994), Deep, low-frequency microearthquakes in or around seismic low-velocity zones beneath active volcanoes in northeastern Japan, *Tectonophysics*, *233*, 233–252, doi:10.1016/0040-1951(94)90243-7.

Hasegawa, A., and J. Nakajima (2004), Geophysical constraints on slab subduction and arc magmatism, in *The State of the Planet: Frontiers and Challenges*, *Geophys. Monogr. Ser.*, vol. 150, edited by R. S. J. Sparks and C. J. Hawkesworth, pp. 81–94, AGU, Washington, D. C.

Hasegawa, A., J. Nakajima, N. Umino, and S. Miura (2005), Deep structure of the northeastern Japan arc and its implications for crustal deformation and shallow seismic activity, *Tectonophysics*, *403*, 59–75, doi:10.1016/j.tecto.2005.03.018.

Hasegawa, A., J. Nakajima, S. Kita, Y. Tsuji, K. Nii, T. Okada, T. Matsuzawa, and D. Zhao (2008), Transportation of H_2O in the NE Japan Subduction Zone as inferred from seismic observations [in Japanese with English abstract and figure caption], *J. Geogr. (Chigaku Zasshi)*, *117*, 59–75, doi:10.5026/jgeography.117.59.

Hashin, Z., and S. Shtrikman (1962), A variational approach to theory of effective magnetic permeability of multiphase materials, *J. App. Phys.*, *33*, 3125–3131, doi:10.1063/1.1728579.

Heise, W., H. M. Bibby, T. G. Caldwell, S. C. Bannister, Y. Ogawa, S. Takakura, and T. Uchida (2007), Melt distribution beneath a young continental rift: The Taupo Volcanic Zone, New Zealand, *Geophys. Res. Lett.*, *34*, L14313, doi:10.1029/2007GL029629.

Honda, S., and M. Saito (2003), Small-scale convection under the back-arc occurring in the low viscosity wedge, *Earth Planet. Sci. Lett.*, *216*, 703–715, doi:10.1016/S0012-821X(03)00537-5.

Honda, S., and T. Yoshida (2005), Application of the model of small-scale convection under the island arc to the NE Honshu subduction zone, *Geochem. Geophys. Geosyst.*, *6*, Q01002, doi:10.1029/2004GC000785.

Huang, Z., D. Zhao, and L. Wang (2011), Seismic heterogeneity and anisotropy of the Honshu arc from the Japan Trench to the Japan Sea, *Geophys. J. Int.*, *184*, 1428–1444, doi:10.1111/j.1365-246X.2011.04934.x.

Hyndman, R. D., and P. M. Shearer (1989), Water in the lower continental crust: Modeling magnetotelluric and seismic reflection results, *Geophys. J. Int.*, *98*, 343–365, doi:10.1111/j.1365-246X.1989.tb03357.x.

Ichihara, H., S. Sakanaka, M. Mishina, M. Uyeshima, T. Nishitani, Y. Ogawa, Y. Yamaya, T. Mogi, K. Amita, and T. Miura (2014), A 3-D electrical resistivity model beneath the focal zone of the 2008 Iwate-Miyagi Nairiku earthquake (M 7.2), *Earth Planets Space*, *66*, 50, doi:10.1186/1880-5981-66-50.

Iwamori, H. (1998), Transportation of H_2O and melting in subduction zones, *Earth Planet. Sci. Lett.*, *160*, 65–80, doi:10.1016/S0012-821X(98)00080-6.

Iwamori, H. (2007), Transportation of H_2O beneath the Japan arcs and its implications for global water circulation, *Chem. Geol.*, *239*, 182–198, doi:10.1016/j.chemgeo.2006.08.011.
Jiracek, G. R. (1990), Near-surface and topographic distortions in electromagnetic induction, *Surv. Geophys.*, *11*, 163–203, doi:10.1007/BF01901659.
Jödicke, H. (1992), Water and graphite in the earth's crust—An approach to interpretation of conductivity models, *Surv. Geophys.*, *13*, 381–407, doi:10.1007/BF01903484.
Jones, C. H., H. Reeg, G. Zandt, H. Gilbert, T. J. Owens, and J. Stachnik (2014), *P*-wave tomography of potential convective downwellings and their source regions, Sierra Nevada, California, *Geosphere*, *10*, 505–533, doi:10.1130/GES00961.1.
Kanda, W., and Y. Ogawa (2014), Three-dimensional electromagnetic imaging of fluids and melts beneath the NE Japan arc revisited by using geomagnetic transfer function data, *Earth Planets Space*, *66*, 39, doi:10.1186/1880-5981-66-39.
Karato, S. (1990), The role of hydrogen in the electrical conductivity of the upper mantle, *Nature*, *347*, 272–273, doi:10.1038/347272a0.
Katz, R. F., M. G. Knepley, B. Smith, M. Spiegelman, and E. T. Coon (2007), Numerical simulation of geodynamic processes with the portable extensible toolkit for scientific computation, *Phys. Earth Planet. Inter.*, *163*, 52–68, doi:10.1016/j.pepi.2007.04.016.
Kawakatsu, H., P. Kumar, Y. Takei, M. Shinohara, T. Kanazawa, E. Araki, and K. Suyehiro (2009), Seismic evidence for sharp lithosphere-asthenosphere boundaries of oceanic plates, *Science*, *24*(324), 499–502, doi:10.1126/science.1169499.
Kelbert, A., G. D. Egbert, and C. deGroot-Hedlin (2012), Crust and upper mantle electrical conductivity beneath the Yellowstone Hotspot Track, *Geology*, *40*, 447–450, doi:10.1130/G32655.1.
Kita, S., T. Okada, A. Hasegawa, J. Nakajima, and T. Matsuzawa (2010), Anomalous deepening of a seismic belt in the upper-plane of the double seismic zone in the Pacific slab beneath the Hokkaido corner: Possible evidence for thermal shielding caused by subducted forearc crust materials, *Earth Planet. Sci. Lett.*, *290*, 415–426, doi:10.1016/j.epsl.2009.12.038.
Kondo, H., K. Tanaka, Y. Mizouchi, and A. Ninomiya (2004), Long-term changes in distribution and chemistry of middle Miocene to Quaternary volcanism in the Chokai-Kurikoma area across the Northeast Japan Arc, *Island Arc*, *13*, 18–46, doi:10.1111/j.1440-1738.2003.00417.x.
Manning, C. E. (1994), The solubility of quartz in H_2O in the lower crust and upper-mantle, *Geochim. Cosmochim. Acta*, *58*, 4831–4839, doi:10.1016/0016-7037(94)90214-3.
Manning, C. E. (2004), The chemistry of subduction-zone fluids, *Earth Planet. Sci. Lett.*, *223*, 1–16, doi:10.1016/j.epsl.2004.04.030.
Matsuno, T., et al. (2010), Upper mantle electrical resistivity structure beneath the central Mariana subduction system, *Geochem. Geophys. Geosyst.*, *11*, Q09003, doi:10.1029/2010GC003101.
McGary, R. S., R. L. Evans, P. E. Wannamaker, J. Elsenbeck, and S. Rondenay (2014), Pathway from subducting slab to surface for melt and fluids beneath Mount Rainier, *Nature*, *511*, 338–341, doi:10.1038/nature13493.
McKenzie, D. (1984), The generation and compaction of partially molten rock, *J. Petrol.*, *25*, 713–765.
Mei, S., and K. L. Kohlstedt (2000a), Influence of water on plastic deformation of olivine aggregates 1. Diffusion creep regime, *J. Geophys. Res.*, *105*, 21,457–21,469, doi:10.1029/2000JB900179.
Mei, S., and K. L. Kohlstedt (2000b), Influence of water on plastic deformation of olivine aggregates 1. Dislocation creep regime, *J. Geophys. Res.*, *105*, 21,471–21,481, doi:10.1029/2000JB900180.
Meqbel, N. M., G. D. Egbert, P. E. Wannamaker, A. Kelbert, and A. Schultz (2014), Deep electrical resistivity structure of the northwestern U.S. derived from 3-D inversion of USArray magnetotelluric data, *Earth Planet. Sci. Lett.*, *402*, 290–304, doi:10.1016/j.epsl.2013.12.026.
Mishina, M. (2009), Distribution of crustal fluids in Northeast Japan as inferred from resistivity surveys, *Gondwana Res.*, *16*, 563–571, doi:10.1016/j.gr.2009.02.005.
Mitsuhata, Y., Y. Ogawa, M. Mishina, T. Kono, T. Yokokura, and T. Uchida (2001), Electromagnetic heterogeneity of the seismogenic region of 1962 M6.5 northern Miyagi earthquake, northeastern Japan, *Geophys. Res. Lett.*, *28*, 4371–4374, doi:10.1029/2001GL013079.
Nakajima, J., and A. Hasegawa (2006), Anomalous low-velocity zone and linear alignment of seismicity along it in the subducted Pacific slab beneath Kanto, Japan: Reactivation of subducted fracture zone?, *Geophys. Res. Lett.*, *33*, L16309, doi:10.1029/2006GL026773.
Nakajima, J., T. Matsuzawa, A. Hasegawa, and D. Zhao (2001), Three-dimensional structure of Vp, Vs, and Vp/Vs beneath northeastern Japan: Implications for arc magmatism and fluids, *J. Geophys. Res.*, *106*, 21,843–21,857, doi:10.1029/2000JB000008.
Nakajima, J., Y. Takei, and A. Hasegawa (2005), Quantitative analysis of the inclined low-velocity zone in the mantle wedge of northeastern Japan: A systematic change of melt-filled pore shapes with depth and its implications for melt migration, *Earth Planet. Sci. Lett.*, *234*, 59–70, doi:10.1016/j.epsl.2005.02.033.
Ni, H., H. Keppler, and H. Behrens (2011), Electrical conductivity of hydrous basaltic melts: Implications for partial melting in the upper mantle, *Contrib. Mineral. Petrol.*, *162*, 637–650, doi:10.1007/s00410-011-0617-4.
Ogawa, Y., T. Yukutake, and H. Utada (1986), Two-dimensional modeling of resistivity structure beneath the Tohoku district, northern Honshu of Japan, by a finite element method, *J. Geomag. Geoelectr.*, *38*, 45–79, doi:10.5636/jgg.38.45.
Ogawa, Y., et al. (2001), Magnetotelluric imaging of fluids in intraplate earthquake zones, NE Japan back arc, *Geophys. Res. Lett.*, *28*, 3741–3744, doi:10.1029/2001GL013269.
Ogawa, Y., M. Ichiki, W. Kanda, M. Mishina, and K. Asamori (2014), Three-dimensional fluid distribution around Naruko volcano, inferred from wide-band magnetotelluric measurement, *Earth Planets Space*, *66*, 158, doi:10.1186/s40623-014-0158-y.
Okada, T., N. Umino, and A. Hasegawa (2010), Deep structure of the Ou mountain range strain concentration zone and the focal area of the 2008 Iwate-Miyagi Nairiku earthquake, NE Japan—Seismogenesis related with magma and crustal fluid, *Earth Planets Space*, *62*, 347–352, doi:10.5047/eps.2009.11.005.
Okada, T., N. Umino, A. Hasegawa, and Group for the aftershock observations of the Iwate-Miyagi Nairiku Earthquake in 2008 (2012), Hypocenter distribution and heterogeneous seismic velocity structure in and around the focal area of the 2008 Iwate-Miyagi Nairiku Earthquake, NE Japan—Possible seismological evidence for a fluid driven compressional inversion earthquake, *Earth Planets Space*, *64*, 717–728, doi:10.5047/eps.2012.03.005.
Okada, T., T. Matsuzawa, J. Nakajima, N. Uchida, M. Yamamoto, S. Hori, T. Kono, T. Nakayama, S. Hirahara, and A. Hasegawa (2014), Seismic velocity structure in and around the Naruko volcano, NE Japan, and its implications for volcanic and seismic activities, *Earth Planets Space*, *66*, 114, doi:10.1186/1880-5981-66-114.
Oldenburg, D. W. (1979), One-dimensional inversion of natural source magnetotelluric observations, *Geophysics*, *44*, 1218–1244, doi:10.1190/1.1441004.
Park, S. K., and M. N. Ducea (2003), Can in situ measurements of mantle electrical conductivity be used to infer properties of partial melts?, *J. Geophys. Res.*, *108*(B5), 2270, doi:10.1029/2002JB001899.
Patro, P. K., and G. D. Egbert (2008), Regional conductivity structure of Cascadia: Preliminary results from 3D inversion of USArray transportable array magnetotelluric data, *Geophys. Res. Lett.*, *35*, L20311, doi:10.1029/2008GL035326.

Pawley, A. R. (1994), The pressure and temperature stability limits of lawsonite—Implications for H_2O recycling in subduction zones, *Contrib. Mineral. Petrol.*, *118*, 99–108, doi:10.1007/BF00310614.
Peacock, S. A. (1990), Fluid processes in subduction zones, *Science*, *248*, 329–337, doi:10.1126/science.248.4953.329.
Poli, S., and M. W. Schmidt (1995), H_2O transport and release in subduction zones—Experimental constraints on basaltic and andesitic systems, *J. Geophys. Res.*, *100*, 22,299–22,314, doi:10.1029/95JB01570.
Rippe, D., M. J. Unsworth, and C. A. Currie (2013), Magnetotelluric constraints on the fluid content in the upper mantle beneath the southern Canadian Cordillera: Implications for rheology, *J. Geophys. Res. Solid Earth*, *118*, 5601–5624, doi:10.1002/jgrb.50255.
Roedder, E. (1984), Fluid inclusions, in *Reviews in Mineralogy*, vol. 12, 646 pp., Miner. Soc. Am., Chantilly, Va.
Schmandt, B., and E. Humphreys (2010), Seismic heterogeneity and small-scale convection in the southern California upper mantle, *Geochem. Geophys. Geosyst.*, *11*, Q05004, doi:10.1029/2010GC003042.
Schmidt, M. W., and S. Poli (1998), Experimentally based water budgets for dehydrating slabs and consequences for arc magma generation, *Earth Planet. Sci. Lett.*, *163*, 361–379, doi:10.1016/S0012-821X(98)00142-3.
Shankland, T. J., and M. E. Ander (1983), Electrical conductivity, temperatures and fluids in the lower crust, *J. Geophys. Res.*, *88*, 9475–9484, doi:10.1029/JB088iB11p09475.
Shimojuku, A., T. Yoshino, and D. Yamazaki (2014), Electrical conductivity of brine-bearing quartzite at 1 GPa: Implications for fluid content and salinity of the crust, *Earth Planets Space*, *66*, 2, doi:10.1186/1880-5981-66-2.
Shumlovich, K. I., B. W. D. Yardley, and C. M. Graham (2006), Solubility of quartz in crustal fluids: Experiments and general equations for salt solutions and H_2O–CO_2 mixtures at 400–800°C and 0.1–0.9 GPa, *Geofluids*, *6*, 154–167, doi:10.1111/j.1468-8123.2006.00140.x.
Siripunvaraporn, W., and G. D. Egbert (2000), An efficient data-subspace inversion method for 2-D magnetotelluric data, *Geophysics*, *65*, 791–803, doi:10.1190/1.14444778.
Siripunvaraporn, W., and G. D. Egbert (2009), WSINV3DMT: Vertical magnetic field transfer function inversion and parallel implementation, *Phys. Earth Planet. Int.*, *173*, 317–329, doi:10.1016/j.pepi.2009.01.013.
Siripunvaraporn, W., G. D. Egbert, Y. Lenbury, and M. Uyeshima (2005), Three-dimensional magnetotelluric inversion: Data-space method, *Phys. Earth Planet. Inter.*, *150*, 3–14, doi:10.1016/j.pepi.2004.08.023.
Takahashi, E. (1980), Thermal history of lehrzolite zenoliths from the Ichinomegata crater, Oga peninsula, northeast Japan, *Geochim. Cosmochim. Acta*, *44*, 1643–1658, doi:10.1016/0016-7037(80)90217-3.
Takahashi, E. (1986), Genesis of calk-alcali andesite magma in a hydrous mantle crust boundary—Petrology of lehrzolite xenoliths from the Ichinomegata crater, Oga peninsula: Northeast Japan. 2, *J. Vol. Geotherm. Res.*, *29*, 355–395, doi:10.1016/0377-0273(86)90051-X.
Tamic, N., H. Behrens, and F. Holtz (2001), The solubility of H_2O and CO_2 in rhyolitic melts in equilibrium with a mixed CO_2-H_2O fluid phase, *Chem. Geol.*, *174*, 333–347, doi:10.1016/S0009-2541(00)00324-7.
Tamura, Y., Y. Tatsumi, D. Zhao, Y. Kido, and H. Shukuno (2002), Hot fingers in the mantle wedge: New insights into magma genesis in subduction zones, *Earth Planet. Sci. Lett.*, *197*, 105–116, doi:10.1016/S0012-821X(02)00465-X.
Tatsumi, Y. (1989), Migration of fluid phases and genesis of basalt magmas in subduction zones, *J. Geophys. Res.*, *94*, 4697–4707, doi:10.1029/JB094iB04p04697.
Tian, Y., and D. Zhao (2012), *P*-wave tomography of the western United States: Insight into the Yellowstone hotspot and the Juan de Fuca slab, *Phys. Earth Planet. Inter.*, *200–201*, 72–84, doi:10.1016/j.pepi.2012.04.004.
Toh, H., K. Baba, M. Ichiki, T. Motobayashi, Y. Ogawa, M. Mishina, and I. Takahashi (2006), Two-dimensional electrical section beneath the eastern margin of Japan Sea, *Geophys. Res. Lett.*, *33*, L22309, doi:10.1029/2006GL027435.
Torres-Verdin, C., and F. X. Bostick (1992), Principles of spatial surface electric field filtering in magnetotellurics: Electromagnetic array profiling (EMAP), *Geophysics*, *57*, 603–622, doi:10.1190/1.1443273.
Tsuchiya, N., and S. Kanisawa (1994), Early Cretaceous Sr-rich silicic magmatism by slab melting in the Kitakami Mountains, northeast Japan, *J. Geophys. Res.*, *99*, 22,205–22,220, doi:10.1029/94JB00458.
Uchida, T. (1993), Smooth 2-D inversion for magnetotelluric data based on statistical criterion ABIC, *J. Geomag. Geoelectr.*, *45*, 841–858, doi:10.5636/jgg.45.841.
Utada, H. (1987), A direct inversion method for two-dimensional modeling in the geomagnetic induction problem PhD thesis, Graduate School of Science, Univ. of Tokyo, Japan.
Uyeshima, M., et al. (2002), Network-MT survey in Japan to determine nation-wide deep electrical conductivity structure, in *Seismotectonics in Convergent Plate Boundary*, edited by Y. Fujinawa and A. Yoshida, pp. 107–121, Terra Scientific Comp., Tokyo, Japan.
Van Keken, P. E., B. R. Hacker, E. M. Syracuse, and G. A. Abers (2011), Subduction factory: 4. Depth-dependent flux of H_2O from subducting slabs worldwide, *J. Geophys. Res.*, *116*, B01401, doi:10.1029/2010JB007922.
Wada, I., M. D. Behn, and J. He (2011), Grain-size distribution in the mantle wedge of subduction zones, *J. Geophys. Res.*, *116*, B10203, doi:10.1029/2011JB008294.
Wannamaker, P. E., et al. (2008), Lithospheric dismemberment and magmatic processes of the Great Basin–Colorado Plateau transition, Utah, implied from magnetotellurics, *Geochem. Geophys. Geosyst.*, *9*, Q05019, doi:10.1029/2007GC001886.
Wannamaker, P. E., T. G. Caldwell, G. R. Jiracek, V. Maris, G. J. Hill, Y. Ogawa, H. M. Bibby, S. L. Bennie, and W. Heise (2009), Fluid and deformation regime of an advancing subduction system at Marlborough, New Zealand, *Nature*, *460*, 733–736, doi:10.1038/nature08204.
Wessel, P., and W. H. F. Smith (1998), New, improved version of generic mapping tools released, *Eos Trans. AGU*, *79*(47), 579, doi:10.1029/98EO00426.
Wilson, C. R., M. Spiegelman, P. E. van Keken, and B. R. Hacker (2014), Fluid flow in subduction zones: The role of solid rheology and compaction pressure, *Earth Planet. Sci. Lett.*, *401*, 261–274, doi:10.1016/j.epsl.2015.05.052.
Wolf, M. B., and P. J. Wyllie (1994), Dehydration-melting of amphibolite at 10 kbar: The effects of temperature and time, *Contrib. Mineral. Petrol.*, *115*, 369–383, doi:10.1007/BF00320972.
Yang, Y., and D. W. Forsyth (2006), Rayleigh wave phase velocities, small-scale convection, and azimuthal anisotropy beneath southern California, *J. Geophys. Res.*, *111*, B07306, doi:10.1029/2005JB004180.
Yoshino, T., K. Mibe, A. Yasuda, and T. Fujii (2002), Wetting properties of anorthite aggregates: Implications for fluid connectivity in continental lower crust, *J. Geophys. Res.*, *107*(B1), 2027, doi:10.1029/2001JB000440.
Yoshino, T., T. Matsuzaki, S. Yamashita, and T. Katsura (2006), Hydrous olivine unable to account for conductivity anomaly at the top of the asthenosphere, *Nature*, *443*, 973–976, doi:10.1038/nature05223.
Zhao, D., A. Hasegawa, and S. Horiuchi (1992), Tomographic imaging of *P* and *S* wave velocity structure beneath northeastern Japan, *J. Geophys. Res.*, *97*, 19,909–19,928, doi:10.1029/92JB00603.
Zhu, G., T. V. Gerya, D. A. Yuen, S. Honda, T. Yoshida, and J. A. D. Connolly (2009), Three-dimensional dynamics of hydrous thermal-chemical plumes in oceanic subduction zones, *Geochem. Geophys. Geosyst.*, *10*, Q11006, doi:10.1029/2009GC002625.